

# Age-resolved chemistry of red giants in the solar neighbourhood

Diane K. Feuillet,<sup>1\*</sup> Jo Bovy,<sup>2,3†</sup> Jon Holtzman,<sup>4</sup> David H. Weinberg,<sup>5</sup>  
 D. A. García-Hernández,<sup>6,7</sup> Fred R. Hearty,<sup>8</sup> Steven R. Majewski,<sup>9</sup>  
 Alexandre Roman-Lopes,<sup>10</sup> Jan Rybizki,<sup>1</sup> Olga Zamora<sup>6,7</sup>

<sup>1</sup>Max-Planck-Institut für Astronomie, Königstuhl 17, D-69117 Heidelberg, Germany

<sup>2</sup>Department of Astronomy and Astrophysics, University of Toronto, 50 St. George Street, Toronto, ON, M5S 3H4, Canada

<sup>3</sup>Dunlap Institute for Astronomy and Astrophysics, University of Toronto, 50 St. George Street, Toronto, Ontario, M5S 3H4, Canada

<sup>4</sup>Department of Astronomy, New Mexico State University, Las Cruces, NM, 88003, USA

<sup>5</sup>Department of Astronomy, The Ohio State University, Columbus, OH, 43210, USA

<sup>6</sup>Instituto de Astrofísica de Canarias, E-38205 La Laguna, Tenerife, Spain

<sup>7</sup>Universidad de La Laguna, Departamento de Astrofísica, E-38205 La Laguna, Tenerife, Spain

<sup>8</sup>Department of Astronomy and Astrophysics, The Pennsylvania State University, University Park, PA 16802, USA

<sup>9</sup>Department of Astronomy, University of Virginia, Charlottesville, VA 22904, USA

<sup>10</sup>Departamento de Física, Facultad de Ciencias, Universidad de La Serena, Cisternas 1200, La Serena, Chile

Accepted XXX. Received YYY; in original form ZZZ

## ABSTRACT

In the age of high-resolution spectroscopic stellar surveys of the Milky Way, the number of stars with detailed abundances of multiple elements is rapidly increasing. These elemental abundances are directly influenced by the evolutionary history of the Galaxy, but this can be difficult to interpret without an absolute timeline of the abundance enrichment. We present age-abundance trends for  $[M/H]$ ,  $[\alpha/M]$ , and 17 individual elements using a sample of 721 solar neighbourhood *Hipparcos* red giant stars observed by APOGEE. These age trends are determined through a Bayesian hierarchical modelling method presented by Feuillet et al. (2016). We confirm that the  $[\alpha/M]$ -age relation in the solar neighbourhood is steep and relatively narrow (0.20 dex age dispersion), as are the  $[O/M]$ - and  $[Mg/M]$ -age relations. The age trend of  $[C/N]$  is steep and smooth, consistent with stellar evolution. The  $[M/H]$ -age relation has a mean age dispersion of 0.28 dex and a complex overall structure. The oldest stars in our sample are those with the lowest and highest metallicities, while the youngest stars are those with solar metallicity. These results provide strong constraints on theoretical models of Galactic chemical evolution (GCE). We compare them to the predictions of one-zone GCE models and multi-zone mixtures, both analytic and numerical. These comparisons support the hypothesis that the solar neighbourhood is composed of stars born at a range of Galactocentric radii, and that the most metal-rich stars likely migrated from a region with earlier and more rapid star formation such as the inner Galaxy.

**Key words:** Galaxy: abundances – Galaxy: evolution – Galaxy: solar neighbourhood – Galaxy: stellar content

## 1 INTRODUCTION

Chemical abundances of stars can tell us a lot about the evolution of the Milky Way and other spiral galaxies. The stellar

populations of the Galactic disc, where star formation has been occurring essentially continuously since its formation, are particularly powerful tools to map the temporal evolution of chemical elements. In order to get a clear picture of how the chemical enrichment happened, we need samples of stars with detailed chemical abundances from different nucleosynthesis channels and ages spanning the full Galac-

\* email: feuillet@mpia.de

† Alfred P. Sloan Fellow

tic disc. High-resolution spectroscopic surveys like the first and second phases of the Apache Point Observatory Galactic Evolution Experiment (APOGEE and APOGEE-2, [Majewski et al. 2017](#)), the Gaia-ESO Survey (GES, [Gilmore et al. 2012](#); [Randich, Gilmore & Consortium 2013](#)), and the Galactic Archaeology with HERMES survey (GALAH, [Freeman et al. 2012](#); [De Silva et al. 2015](#); [Martell et al. 2017](#)) are providing atmospheric parameters and measurements of multiple elemental abundances for large samples of stars throughout the Galaxy. In conjunction, the Gaia mission ([Gaia Collaboration et al. 2016](#)) is providing astrometric measurements for these same stars.

While these surveys result in an unprecedented sample of stars with abundance measurements across a huge range of distances with which the structure of stellar populations of different abundances can be mapped precisely ([Bovy et al. 2012, 2016](#)), the complexity of Galactic chemical evolution (GCE) makes the interpretation of the global enrichment history difficult. The time-scales of the chemical enrichment histories of stellar populations are greatly affected by the local star formation history and gas inflow/outflow (e.g. [Chiappini, Matteucci & Gratton 1997](#); [Dalcanton 2007](#); [Finlator & Davé 2008](#)). It has also been shown that the migration of stars away from their birth radius while conserving the orbit’s eccentricity could be a significant process in the Galaxy (see [Wielen et al. 1996](#); [Sellwood & Binney 2002](#); [Schönrich & Binney 2009](#); [Loebman et al. 2011](#)). This process of radial migration would result in an observed chemical abundance distribution at a given radius that has been altered from that of the native population. The change in shape of the observed disc metallicity distribution function (MDF), from negatively skewed in the inner Galaxy to positively skewed in the outer Galaxy, provides further strong circumstantial evidence for this effect ([Hayden et al. 2015](#); [Loebman et al. 2016](#)).

Perhaps due to these complications from an evolutionary history that is not well known, recent studies have found that the traditionally discussed ‘thick’ and ‘thin’ Milky Way disk populations are not as separate in their spatial, kinematic, abundance, and age distributions as previously thought (e.g. [Bensby et al. 2014](#); [Hayden et al. 2017](#)). Instead of the canonical ‘thick’ and ‘thin’ disk populations, in this work we occasionally refer to the high- and low- $\alpha$  sequences, with the high- $\alpha$  sequence equating more closely to the canonical ‘thick’ disk and the low- $\alpha$  sequence equating more closely to the canonical ‘thin’ disk. These terms convey the directly observable quality of the two apparent sequences in the  $[\alpha/M]$  vs  $[M/H]$  distribution.<sup>1</sup>

In order to compare the stellar populations across the disc on a Galactic scale and build a cohesive picture of Galactic evolution from chemical abundances and astrometry, we need stellar age measurements to place all the stars on an absolute timeline. However, stellar ages are difficult to determine for large samples of field stars, such as those provided by the current high-resolution spectroscopic surveys. While asteroseismology can provide precise ages (see [Chaplin et al. 2011](#)), it requires high time-cadence observations,

and is not currently possible for the full spectroscopic samples of hundreds of thousands of stars. Isochrone matching to spectroscopically derived atmospheric parameters can provide reasonable age estimates for main sequence turn off and subgiant stars (e.g. [Haywood et al. 2013](#); [Bensby, Feltzing & Oey 2014](#)), but the age uncertainties become large ( $\sim 0.25$  dex) for red giant stars if only spectroscopic parameters are known (see [Feuillet et al. 2016](#), hereafter F16). Although more precise ages can be determined for subgiants, this is a relatively brief stage of stellar evolution, and the higher luminosity of red giants makes them better suited to probing the full Galactic disc and bulge. As a result, samples of field stars with age determinations have been fairly small and have not extended far beyond  $\sim 1$  kpc of the Sun, or the *Kepler* and CoRoT fields (e.g. [Chaplin et al. 2011](#); [Anders et al. 2017](#)). The exceptions to this limitation are the recent studies that have pushed out farther into the Galactic disc using C and N abundance ratios as a proxy for mass/age in red giants ([Masseron & Gilmore 2015](#); [Martig et al. 2016](#); [Ness et al. 2016](#)). This CN age method has been used to map the stellar populations structure in age and abundance for a large sample of stars ([Mackereth et al. 2017](#)). However, this method does require calibration either to models or empirically to samples with precise ages, as well as a correction for potential Galactic gradients in C and N. Therefore techniques directly connected to stellar physics that do not rely on elemental abundances are preferable. Fortunately, the age estimate of field stars, particularly subgiants and giants, can be greatly improved if the distance, and therefore the luminosity, is known. Soon the number of stars for which ages can be determined will greatly increase with the availability of parallax measurements from Gaia ([Gaia Collaboration et al. 2016](#)).

Much work has been done trying to determine whether an age-metallicity relation exists for stars in the solar neighbourhood (e.g. [Edvardsson et al. 1993](#); [Nordström et al. 2004](#); [Bergemann et al. 2014](#)), and recent studies have found  $\alpha$ -element enhancement, i.e.  $[\alpha/M]$ , to have a tighter correlation with age than metallicity,  $[M/H]$  ([Haywood et al. 2013](#); [Bensby et al. 2014](#)). From these previous observational studies as well as studies of GCE models (e.g. [Chiappini et al. 1997](#); [Minchev et al. 2013](#)), it appears that the  $[\alpha/M]$ – $[M/H]$ –age or kinematics–age space is a better diagnostic for the evolution of the high- and low- $\alpha$  sequences. Using large samples of stars with CN ages or asteroseismology, recent work has found that the mean age of the high- $\alpha$  sequence is distinctly older than the mean age of the low- $\alpha$  sequence, and that there is little age evolution with increasing  $[M/H]$  and decreasing  $[\alpha/M]$  along the high- $\alpha$  sequence ([Ness et al. 2016](#); [Ho et al. 2017](#); [Wu et al. 2017](#), with age uncertainties of 0.2, 0.2, and 0.1 dex, respectively). This suggests that the high- $\alpha$  sequence formed rapidly, and almost entirely before the low- $\alpha$  sequence.

Until very recently, few studies have looked at the relationship between age and individual elemental abundance for more than one or two elements. [Spina et al. \(2016\)](#), [Adibekyan et al. \(2016\)](#), and [Bedell et al. \(2018\)](#) have explored trends of age with individual abundances of solar-type stars, inspired by the strong, linear correlation between age and the  $[Y/Mg]$  abundance ratio of solar twins found by [da Silva et al. \(2012\)](#) and [Nissen \(2015\)](#) (see also [Feltzing et al. 2017](#); [Slumstrup et al. 2017](#)). These studies analysed

<sup>1</sup> We discuss the precise meaning of M below, but roughly speaking  $[M/H]$  refers to the abundance of iron-peak elements and  $[\alpha/M]$  refers to the abundance of  $\alpha$ -elements relative to iron-peak.

small samples of dwarf stars (a few 100 at most) and highlighted the discovery that certain abundance indicators can be used as chemical clocks (see also Van Eck et al. 2015). While these tight age-abundance relations are extremely interesting and potentially very useful, they have not been tested beyond the solar neighbourhood where conditions of star formation were likely different. Here we focus on a larger sample of red giant stars ( $\sim 700$ ), and the aim of the present work is not primarily to find an abundance ratio that can be used as a proxy for age, but rather to characterise the enrichment of the individual elements with time for the purposes of constraining the parameters of Galactic evolution such as radial migration, gas inflow, and gas mixing in the disc, as well as nucleosynthetic yields.

Jia et al. (2018) use the sample presented in F16 combined with the APOGEE Data Release 13 (DR13) elemental abundances to examine the age-abundance trends for Fe, Si, K, Ca, Mn, and Ni. They use the ages derived from the spectrophotometric mass and the red giant mass-age relation, which have uncertainties of 0.38 dex in  $\log(\text{age})$ . Jia et al. (2018) find a large spread in abundance at all but the youngest ages, and that all but one of the most enhanced stars in  $[\text{Si}/\text{M}]$  and  $[\text{Ca}/\text{M}]$  are old. Smaller age uncertainties are possible for this sample using a Bayesian isochrone matching approach as discussed below and in F16.

In this paper, we use the sample of solar neighbourhood red giant stars observed using the New Mexico State University (NMSU) 1-m + APOGEE set-up presented by F16 to examine the trends of individual elemental abundance with age in the solar neighbourhood. This work is improving the analysis by using updated spectroscopic parameters and modeling the abundance-age trends as a function of each individual element, instead of just  $[\alpha/\text{M}]$ . We find an interesting turn over in the age-metallicity relation at high metallicities. The trends of most of the individual  $\alpha$ -elements are consistent with the overall  $[\alpha/\text{M}]$  trend. The hierarchical modeling method is briefly outlined in Section 2, and fully described in F16. In Section 3, we present the age-abundance trends for  $[\text{M}/\text{H}]$ ,  $[\alpha/\text{M}]$ , and 17 individual elements. In Section 4, we present some GCE models for qualitative interpretation of these observations. We summarise our findings in Section 5.

## 2 METHOD

### 2.1 Observed sample

We use a sample of 721 local red giant stars observed with the NMSU 1-m + APOGEE capability presented in F16. These stars were selected to have  $(J-K)_0 > 0.5$ , an absolute 2MASS  $H$  magnitude brighter than 2, and a Hipparcos parallax error less than 10 per cent (van Leeuwen 2007). The distance measurement is critical because, as was shown in F16, using the absolute magnitude in addition to the spectroscopic parameters to determine the age of giants reduces age uncertainties by  $\sim 0.07$  dex.

In this work we use APOGEE calibrated atmospheric parameters and chemical abundances from the Sloan Digital Sky Survey IV (SDSS-IV, Blanton et al. 2017; Gunn et al. 2006) Data Release 14 (DR14, Abolfathi et al. 2017). The APOGEE target selection is described in Zasowski et al.

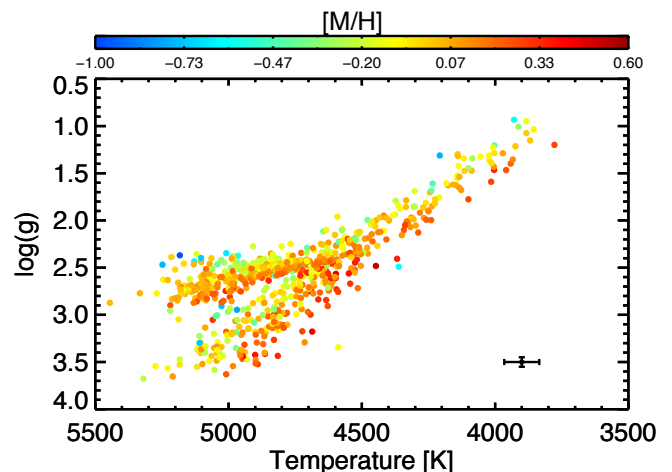


**Figure 1.** The spectroscopic Hertzsprung–Russell Diagram of the sample with DR14 parameters. The colour indicates the metallicity. The typical uncertainty is shown in the bottom right corner.

(2013) and data reduction is described in Nidever et al. (2015). The atmospheric parameters and chemical abundances are determined using the APOGEE Stellar Parameters and Chemical Abundances Pipeline (ASPCAP, García Pérez et al. 2016). ASPCAP uses the code FERRE (Allende Prieto et al. 2006) in combination with grids of normalised stellar synthetic spectra (see Zamora et al. 2015), as created with extensive atomic and molecular line lists (Shetrone et al. 2015), to simultaneously determine  $T_{\text{eff}}$ ,  $\log g$ ,  $[\text{M}/\text{H}]$ ,  $[\alpha/\text{M}]$ ,  $[\text{C}/\text{M}]$ ,  $[\text{N}/\text{M}]$ , and microturbulence through  $\chi^2$  minimization. During this process, ASPCAP fits for the overall abundance of metals  $[\text{M}/\text{H}]$  and the relative abundance of  $\alpha$ -elements  $[\alpha/\text{M}]$ , using O, Mg, Si, S, Ca, and Ti; the relative abundances of non- $\alpha$  elements (except for C and N) are set to solar ratios when inferring  $[\text{M}/\text{H}]$ . The measurements of both  $[\text{M}/\text{H}]$  and  $[\alpha/\text{M}]$  are dominated by different elements in different temperature regimes. The abundances of the individual elements are then determined by fitting specific spectral windows containing relevant absorption lines while varying the corresponding family of elements (Holtzman et al. 2015, 2018, in preparation). The DR14 abundances have been internally calibrated to remove  $T_{\text{eff}}$  correlations in open clusters, similar to the corrections to DR12 described in Holtzman et al. (2015); see Holtzman (2018, in preparation) for a description of the DR14 calibrations. The APOGEE team has found that the metallicity parameter  $[\text{M}/\text{H}]$  closely correlates with the  $[\text{Fe}/\text{H}]$  measurement (Holtzman et al. 2015, 2018, in preparation). In this paper we will assume that the ASPCAP measurements of  $[\text{M}/\text{H}]$  and  $[\alpha/\text{M}]$  can be taken as proxies from  $[\text{Fe}/\text{H}]$  and  $[\alpha/\text{Fe}]$ , and therefore compared to literature results and theoretical models for these ratios.

In Fig. 1 we display the spectroscopic Hertzsprung–Russell (HR) diagram colored by  $[\text{M}/\text{H}]$  for our sample using DR14 calibrated parameters. In F16, we applied separate calibrations of the surface gravities ( $\log g$ ) for red clump (RC) stars and first-ascent red giants but, this additional correction has been included in the internal APOGEE DR14 calibrations. Through comparisons to asteroseismic  $\log g$  measurements, it has been found that the  $\log g$  of

massive secondary clump stars (mass  $> 1.5M_{\odot}$ ) has been overcorrected in DR14 by up to 0.2 dex and the true  $\log g$  is higher. While we do not have seismic information about the evolutionary stage of our stars, we use the mass calculations from F16 (with uncertainties of 0.11 dex,  $\sim 30\%$ ) and the position in  $T_{\text{eff}}$  vs  $\log g$  space to determine that our sample has roughly 150 stars that could be affected by this  $\log g$  overcorrection. A higher  $\log g$  in the secondary clump stars would cause the age estimation from Bayesian isochrone matching to be younger. Therefore our age estimates for the massive secondary clump stars could be too old. We discuss below how this might affect each of our observed abundance-age trends in §3. We refer the reader to Holtzman (2018, in preparation) for a full discussion of the DR14 analysis and calibrations.

We use updated parallax measurements from the *Tycho-Gaia* Astrometric Solution catalogue (TGAS, Lindegren et al. 2016; Brown 2017) for those stars in TGAS with smaller uncertainties than the Hipparcos measurement. Approximately 60 per cent of the stars in our sample are included in TGAS, the remaining stars are too bright for this catalogue. If the TGAS parallax uncertainty is smaller than the Hipparcos uncertainty from Anderson et al. (2012), then we use the TGAS parallax and uncertainty. There are now approximately 150 additional giant stars in APOGEE with TGAS parallax uncertainties below 10 per cent that were not included in the F16 sample, but there is a dependence in the TGAS parallax uncertainty on  $\log g$ , because lower  $\log g$  stars are typically more distant and therefore have larger relative TGAS parallax uncertainties. To avoid biasing our sample due to our parallax uncertainty cut, we do not include these additional stars in our analysis. For future analyses of larger samples of APOGEE-*Gaia* stars, a full characterisation of this  $\log g$  bias will be needed.

## 2.2 Age determination

We first redo the Bayesian isochrone matching analysis using the DR14 parameters. Following the method described in F16, we calculate the age probability distribution function (PDF) for each star using a simple Bayesian isochrone matching to effective temperature ( $T_{\text{eff}}$ ), surface gravity ( $\log g$ ),  $[M/H]$ , and absolute Tycho *V*-band magnitude ( $M_{V_T}$ ). We assume a Chabrier lognormal initial mass function (IMF, Chabrier 2001), a metallicity distribution function that is flat within the uncertainties of  $[M/H]$ , and a flat star formation history (SFH) in  $\log(\text{age})$ , as dictated by the isochrone age grid.

The full age PDFs for each star using DR14 parameters are available online through the public data repository Zenodo (DOI:10.5281/zenodo.1199541). As in F16, these age PDFs are often highly non-Gaussian with multiple peaks or a significant tail to large or small ages. A single age from the simple Bayesian isochrone matching is determined to be the probability weighted mean of the age PDF. The right panel of Fig. 2 shows the  $[\alpha/M]$  vs  $[M/H]$  figure colored by this Bayesian age. We show these ages to give a sense of the age distribution with  $[\alpha/M]$  and  $[M/H]$  independent of the hierarchical modeling, but we note that the median uncertainty on these Bayesian ages is 0.16 dex in  $\log(\text{age})$  or  $\sim 2$  Gyr at an age of 5 Gyr.

To produce more robust age-abundance trends than is

possible using the ages of individual stars determined as the mean of the Bayesian age PDF, we use the hierarchical modeling technique presented in F16. This method uses the full age PDFs produced by a simple Bayesian isochrone matching to constrain the parameters of a model SFH. By using the combined age PDFs of mono-abundance stars we are able to preserve the information in the individual non-Gaussian PDFs, which is lost when a single mean age is taken instead. As in F16, we use a Gaussian + uniform model SFH to determine the mean age and age dispersion of the mono-abundance sample. These parameters are determined to be the most likely mean and dispersion of the Gaussian function and are not strongly influenced by any outlier stars. For a mono-abundance sample in which most of the age PDFs peak at very different ages, the dispersion of the Gaussian will be large. By contrast, a mono-abundance sample in which most of the age PDFs peak at a similar age and only a few PDFs peak at a different age, the dispersion will be small and the presence of the outlier stars will not be obvious from the SFH parameters. This model is a Gaussian in  $\log(\text{age})$  with a prior probability of 7.5 per cent that a given star is drawn from a uniform distribution in  $\log(\text{age})$  instead of the Gaussian distribution, allowing for outlier stars. The choice of 7.5 per cent for the outlier fraction is arbitrary, but we find the exact value does not have a large effect on the Gaussian parameters. The outlier fraction is more important when using the modeled SFH to find individual ages of stars. An outlier fraction of 15 per cent produces the same SFH parameters as 7.5 per cent. In F16, the SFH model was fit to subsamples of stars with a single  $[\alpha/M]$ , but here we also fit the model SFH to subsamples in bins of  $[M/H]$  and the individual  $[X/M]$  abundance ratios. An independent hierarchical model is created for each element, resulting in different SFH models.

To create the abundance bins for each element the stars are sorted by the given abundance, then starting at one abundance edge a bin is created with some minimum width in abundance. However, if fewer than 15 stars are contained within the minimum bin width, the bin is expanded until it contains 15 stars. Here, the minimum bin width is set to be the mean uncertainty in the abundances of each element. We tested using different bin widths and minimum numbers of stars and find that the results produced similar trends regardless of binning. We also found the results were robust against binning from low to high abundance versus high to low abundance. We present results binned from low to high abundance, therefore the lowest abundance bin can be strongly influenced by stars with anomalously low abundances, and the highest abundance stars are sometimes not included due to a lack of stars. It should be noted that full systematic uncertainties due to spectroscopic methods and stellar models are not included in our analysis. For a full description of the hierarchical modeling analysis techniques, we refer the reader to F16.

## 3 AGE TRENDS

### 3.1 $[\alpha/M]$ and overall metallicity

In F16, we found that the mean age of stars steeply increases with  $[\alpha/M]$ . This result is reproduced here in Fig. 2

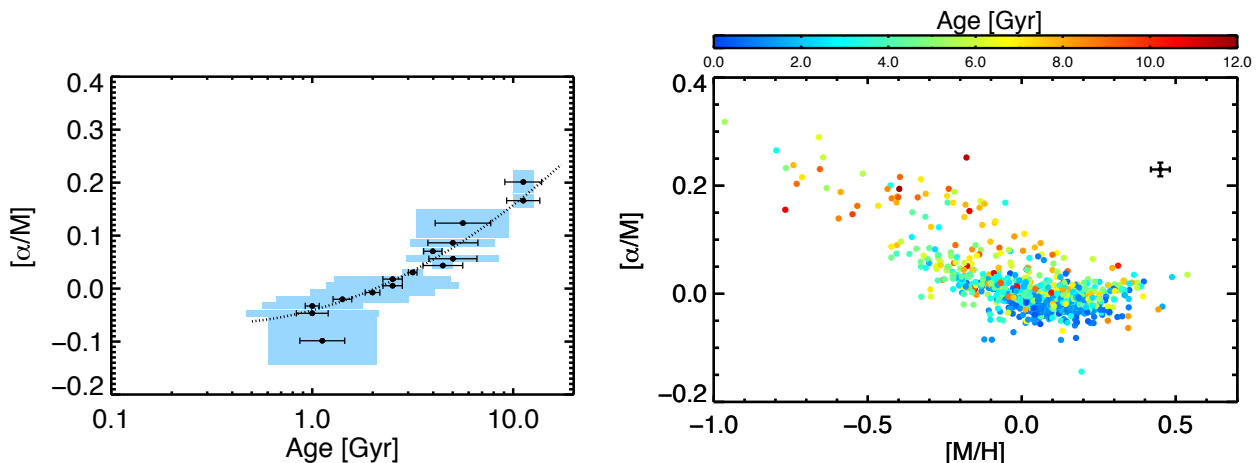


**Figure 2.** Left: The parameters of a Gaussian+uniform model SFH determined as a function of  $[\alpha/M]$ . The points indicate the mean age of the SFH and the mean bin  $[\alpha/M]$ . The error bars indicate the uncertainty in the mean age parameter. The shaded region indicates the age dispersion of the model SFH and abundance range of the bin. We indicate a quadratic fit to the  $[\alpha/M]$ -log(age) relation used for comparison to other elements with the dotted line, see Equation 1. Right: The  $[\alpha/M]$  vs  $[M/H]$  distribution of the sample using DR14 parameters, colored by the simple Bayesian age before hierarchical modeling is done. A typical error bar is shown in the top right corner.

using DR14  $[\alpha/M]$  values. In this figure, the points indicate the mean age of the model SFH as a function of the  $[\alpha/M]$  bin. The error bars indicate the uncertainty in the mean age parameter. This uncertainty is given as the variance in the probability distribution function of the mean age parameter. The blue shaded regions indicate the value of the age dispersion parameter for the model SFH and the range of the abundance bin. All figures with the mean hierarchical age on the  $x$ -axis are shown as linear age with a log scale. This choice is to allow for easier comparisons with other studies while retaining the scale used in the hierarchical modeling method.

The resulting  $[\alpha/M]$  trend using DR14 values is qualitatively the same as in F16 using DR12 values, showing a steep increase in mean age with  $[\alpha/M]$ , even at young ages. Recent studies have found a steepening of the age- $[\alpha/M]$  relation at older ages (see e.g. Haywood et al. 2013; Bergemann et al. 2014), which is in agreement with our results. We also find that the lower  $[\alpha/M]$  bins have larger age dispersions, indicating a larger range of ages represented by lower  $[\alpha/M]$  stars, which is consistent with previous studies (e.g. Ramírez, Allende Prieto & Lambert 2013; Haywood et al. 2013; Bensby et al. 2014; Hayden et al. 2017). The dotted line in Fig. 2 indicates a fit to the  $[\alpha/M]$ -age relation used to compare the  $[\alpha/M]$  trend with other elements in the figures below. The equation used is quadratic in  $\log(\text{age})$  [yr],  $\tau$ :

$$[\alpha/M] = 7.0589 - 1.6775\tau + 0.0987\tau^2. \quad (1)$$

The right panel of Fig. 2 shows the  $[\alpha/M]$  vs  $[M/H]$  distribution of this sample, colored by the single age determined as the mean of the simple Bayesian isochrone matching. The age used here is the mean of the Bayesian age PDF, and is not yet informed by the hierarchical modeling. The typical  $[\alpha/M]$  and  $[M/H]$  uncertainty is indicated in the top right corner. The typical age uncertainty in the Bayesian age is 0.16 dex. The trend between  $[\alpha/M]$  and age can be recovered by eye from this figure, but due to the large age uncertainties and non-Gaussian Bayesian age PDFs, it is much more clear when the hierarchical modeling is done.

Fig. 3 shows the results of a model SFH constrained as a function of  $[M/H]$  in the left panel and  $[O/H]$  in the right panel.  $[M/H]$  is a more complicated tracer of Galactic chemical evolution than the  $\alpha$ -elements due to the contributions to  $[M/H]$  from both core-collapse supernovae and type Ia supernovae. Therefore, we also examine  $[O/H]$  as a tracer of the overall metallicity. The age trends with  $[M/H]$  and  $[O/H]$  are similar. We find that the mean age is oldest for the most metal-poor stars in our sample and decreases with increasing metallicity until solar metallicity. We see a turn over in the age-metallicity relation above solar metallicity so that the most metal-rich stars have a mean age that is older than the solar metallicity stars. Fig. 2 shows the  $[\alpha/M]$  vs  $[M/H]$  distribution for the sample. The distribution of the low- $\alpha$  sequence shows an upturn in  $[\alpha/M]$  above solar metallicity. The most metal-rich stars actually have solar  $[\alpha/M]$ , and therefore have an age consistent with the steep and smooth age increase with  $[\alpha/M]$ . This observation that the most metal-rich stars are not the youngest stars is consistent with observations from the Geneva-Copenhagen Survey (see fig. 16 of Casagrande et al. 2011), which find the metal-rich end of the solar neighbourhood metallicity distribution function is dominated by intermediate-age and old stars. This is also consistent with fig. 17 of F16, which shows that the younger stars have a smaller spread in metallicity and that the most metal-rich stars actually have intermediate ages of 1–4 Gyr.

In Fig. 3 we see a large age dispersion at all metallicities, suggesting a broadly peaked age distribution. This is also observed by other studies of the solar neighbourhood, which find a large spread in metallicity at all ages (see Edvardsson et al. 1993; Bensby et al. 2014; Bergemann et al. 2014; Mackereth et al. 2017). The results of Ness et al. (2016), Ho et al. (2017), and Wu et al. (2017) suggest that this broad age distribution at a given  $[M/H]$  should be double-peaked and a function of  $[\alpha/M]$  due to the presence of the older, high- $\alpha$  sequence and the younger low- $\alpha$  sequence.

We further investigate the  $[\alpha/M]$ - $[M/H]$ -age space by performing a hierarchical modeling on stars with similar

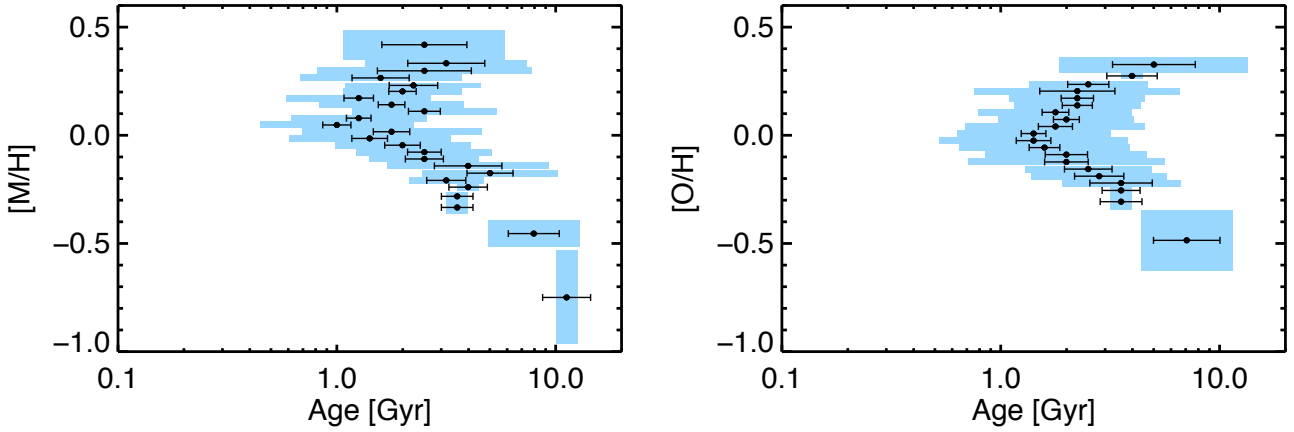


**Figure 3.** The same as left panel of Fig. 2 but for  $[M/H]$  and  $[O/H]$ . In  $[M/H]$  and  $[O/H]$ , both the lowest abundance and highest abundance stars are older than the solar abundance stars.

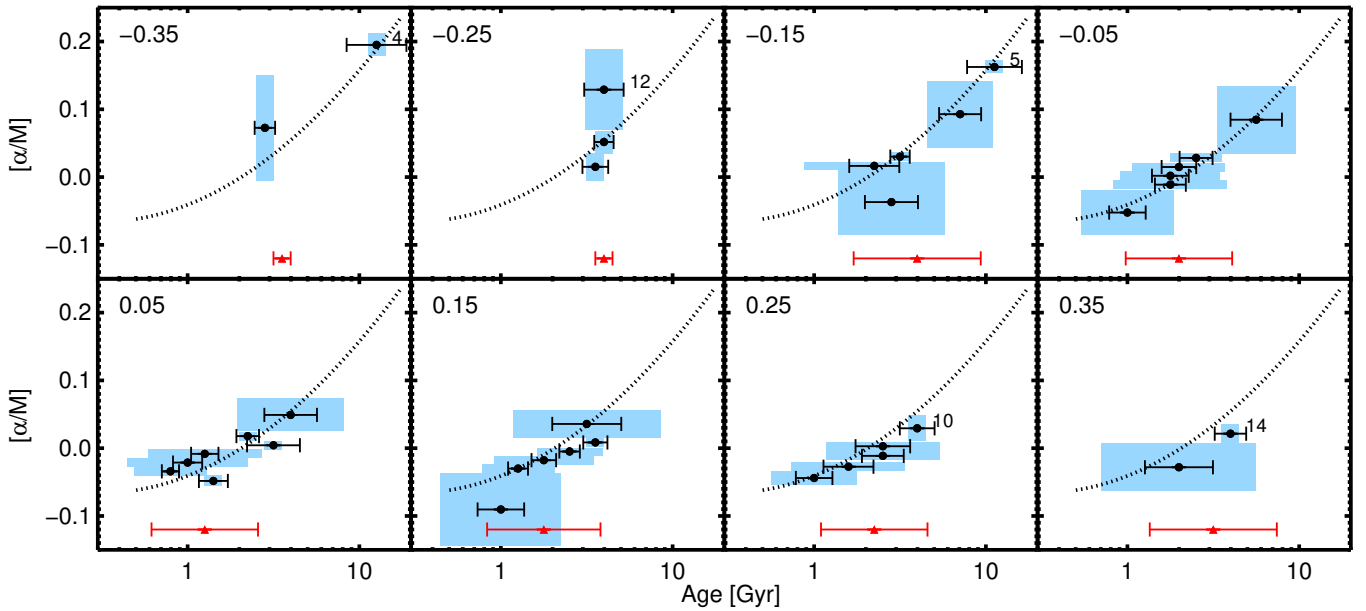


**Figure 4.** Hierarchical modeling of the SFH as a function of both  $[M/H]$  and  $[\alpha/M]$ . Each panel gives the  $[\alpha/M]$ -age relation within a single  $[M/H]$  bin. The point gives the mean age and the error bars indicate the uncertainty in the mean. The blue shaded region indicates the age dispersion and the abundance width. For points with fewer than 15 stars, the number of stars used is given next to the point. The  $[M/H]$  bins are 0.1 dex wide and the central value is shown in the upper left corner of the panel. The fit to the overall  $[\alpha/M]$ -age relation in Fig. 2 and Equation 1 is shown by the dotted line. In the bottom of each panel in red is given the mean age and age dispersion of the  $[M/H]$  bin from Fig. 3 that is closest to the panel central metallicity. The binning in metallicity was done differently in these two figures, therefore there is not a directly corresponding bin for each panel.

$[\alpha/M]$  and  $[M/H]$  abundances. To do this, we first bin the stars by  $[M/H]$ , using bins with a constant width of 0.1 dex. Within each  $[M/H]$  bin, we bin in  $[\alpha/M]$  using at least 15 stars in each bin and a minimum bin width equal to the mean ASPCAP uncertainty in  $[\alpha/M]$ , in the same way as is done in Fig. 2. The results of this exercise are shown in Fig. 4. Each panel shows the  $[\alpha/M]$ -age relation for a single  $[M/H]$  bin. The bin central  $[M/H]$  is given in the upper left corner of each panel. The points indicate the mean age and the error bars indicate the uncertainty in the mean. The blue shaded region shows the age dispersion and the abundance width. Due to the small number of high  $[\alpha/M]$  stars in our sample, the highest  $[\alpha/M]$  bins do not all contain 15 stars,

but we show these bins in order to get a sense of the age distribution across the sample. For bins with fewer than 15 stars, the number of stars is indicated next to the point in Fig. 4. The fit to the overall  $[\alpha/M]$ -age relation, see Equation 1, is shown by the dotted line. At the bottom of each panel there is a point in red. This is the mean age and age dispersion of the overall  $[M/H]$ -age relation bin from Fig. 3 that is closest to the bin central metallicity. Because the binning in metallicity was done differently in the two figures, there is not always a corresponding  $[M/H]$  bin between Fig. 3 and 4.

It is clear from this figure that the large spread in the age metallicity relation seen in Fig. 3 is due to a spread

in  $[\alpha/M]$  at each metallicity, and that, on average, the high  $[\alpha/M]$  stars are older than the low  $[\alpha/M]$  at the same  $[M/H]$ . In Fig. 4 it can be seen that at any given metallicity there is a range in both  $[\alpha/M]$  and age, which generally follows the same  $[\alpha/M]$ –age relation that is found using the full sample. There could be outliers to this general trend in our sample, such as the young  $\alpha$ -rich stars noted by Martig et al. (2015) and Chiappini et al. (2015). In F16, we noted the presence of some young  $[\alpha/M]$ -rich stars. Using the hierarchical modeling method, we obtain only the mean age and age distribution of the model SFH and not ages of individual stars. In our sample we find a small age dispersion in the highest  $[\alpha/M]$  bins suggesting there are very few intermediate or young stars at these abundances. However, the bins lower than  $[\alpha/M]=0.15$  have larger age dispersions, which could be caused by the presence of young  $[\alpha/M]$ -rich stars.

Separating the metal-rich stars into high- and low- $\alpha$  subsets does not reveal any truly young population at the highest metallicities that could have been dominated by older, high- $[\alpha/M]$  stars. In Fig. 4, as in Fig. 3, the youngest stars have solar metallicity. The most metal-rich stars are unlikely to be a continuation of simple star formation in the solar neighbourhood as might be expected from their metallicity alone due to their older age and slightly higher  $[\alpha/M]$  than the solar metallicity stars. In addition, observations of young B-stars in the solar neighbourhood, which reflect the present-day interstellar medium, reveal solar metallicities (e.g. Nieva & Przybilla 2012). This suggests that the metal-rich stars must have formed elsewhere. These stars could have formed outside of the solar neighbourhood, perhaps the inner Galaxy where the mean  $[M/H]$  of stars is observed to be higher, and radially migrated to the solar radius. This is consistent with the behavior of the radial ‘donut’ profile found by Bovy et al. (2016) and Mackereth et al. (2017) using APOGEE observations of the disc. In these studies, the density profiles of the most metal-rich stars peaks in the inner Galaxy, suggesting that most metal-rich stars were formed inside the solar neighbourhood. In the full chemo-dynamical model of the Milky Way presented by Minchev, Chiappini & Martig (2013), the metal-rich end of the solar neighbourhood metallicity distribution function is composed primarily of stars born at a galactocentric radius of 3–5 kpc, see their fig. 3. In the model, stars born at this radius have primarily intermediate to old ages. We discuss comparisons of our observed age–metallicity trend to multi-zone analytic chemical evolution models in Section 4.1.

It is interesting to note that there is some discontinuity in the age–metallicity relation between  $[M/H]$  of  $-0.4$  and  $-0.2$  in Fig. 3. Four metallicity bins have ages younger than the general trend suggests, and also lower age dispersions. At  $[M/H]$  of  $-0.4$  the low- $\alpha$  sequence starts, and by  $[M/H]$  of  $-0.2$ , the low- $\alpha$  sequence strongly dominates the metallicity bin, see Fig. 2. These four bins also have smaller age dispersions than the other metallicity bins, suggesting that at  $[M/H]$  between  $-0.4$  and  $-0.2$ , the stars in the high- and low- $\alpha$  sequences have comparable ages. Indeed, in Fig. 4 the metallicity bin from  $-0.3$  to  $-0.2$  shows a very similar mean age at both high and low  $[\alpha/M]$ . Again, we note that in our sample there are very few  $\alpha$ -enhanced stars and more stars are needed to do a robust analysis on single  $[\alpha/M]$ , single  $[M/H]$  bins. The discontinuity at low abundances is

not strong in the  $[O/H]$  age trend, but the age dispersions in the bins around  $[O/H]$  of  $-0.3$  are also significantly smaller.

An important question when trying to interpret the observed  $[M/H]$ –age and  $[\alpha/M]$ –age relations is why the  $[M/H]$ –age relation is strongly affected by the possible radial migration, while the  $[\alpha/M]$ –age relation remains relatively steep and narrow. We include some discussion of this issue in §4.1, but high-resolution models and larger observational samples with smaller age uncertainties are needed to fully address this issue.

The position of the Sun in the abundance–age relations of  $[\alpha/M]$ ,  $[M/H]$ , and  $[O/H]$  (as well as most of the individual elements) is older than the age dispersion range of the solar abundance bin, assuming a solar age estimate of 4.66 Gyr from Dziembowski et al. (1999). This may indicate that our age estimates are systematically too young. But this is only a systematic shift in the absolute age value and the relative ages are still reliable. Alternatively, this could mean that the Sun is a significant outlier in the solar neighborhood. The Sun would also lie on the older edge of the  $[\alpha/M]$ –age distribution of solar neighbourhood stars found by Haywood et al. (2013). It is also older than the mean age of the solar bin in the  $[\alpha/M]$ – $[M/H]$ –age figures of Martig et al. (2016), Ho et al. (2017), and Wu et al. (2017), but these samples are much larger and extend beyond the solar neighborhood. The Sun as an outlier is not consistent with the  $[\alpha/M]$ –age relations found by Bensby et al. (2014) and Bergemann et al. (2014), or with any age–metallicity relations from the literature. The young B-star observations of (Nieva & Przybilla 2012) lend support to our observation that the youngest stars in the solar neighbourhood, are indeed those with solar metallicities. This suggests at least that the Sun was not born in the solar neighbourhood given its intermediate age and solar metallicity. Models of Galactic evolution have shown that the Sun has likely migrated 1–4 kpc from its birth radius (e.g. Wielen et al. 1996; Minchev et al. 2013). However, other stars with similar ages and abundances to the Sun could have also migrated into the solar neighbourhood.

### 3.2 Carbon and Nitrogen

Carbon and nitrogen abundances in the atmospheres of red giant stars are affected by internal mixing of material during the first dredge-up phase. During this phase, the convective envelope extends into the H-burning region in the core and brings enriched material to the stellar atmosphere (Iben 1965). This material from the core has been enriched through the CN cycle, which results in a build up of N and a depletion of C. The depth of the convective zone during the first dredge-up phase is dependent on the mass of the star, resulting in decreasing atmospheric C to N ratios in higher mass red giants (see Salaris et al. (2015) for a detailed explanation).

The left panels of Fig. 5 show the parameters of a SFH model constrained as a function of  $[C/M]$  and  $[N/M]$ . Because the C and N surface abundance ratio in giants are actually a function of mass and only manifest as a correlation with age due to the tight mass–age relation for red giant stars, we also show the results of the hierarchical modelling as a function of inferred mass in the middle panels. For each abundance ratio bin we compute the average mass and mass

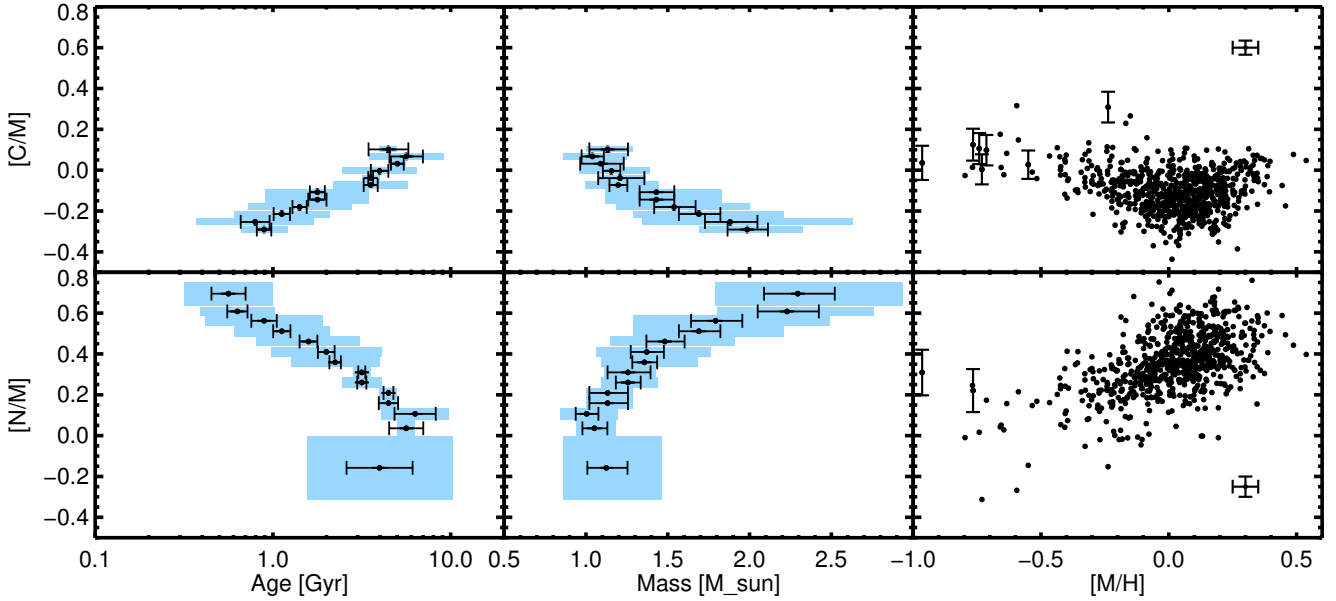


**Figure 5.** The left panels are the same as the left panel of Fig. 2 but for  $[C/M]$  and  $[N/M]$ . The middle panels show the result of the hierarchical modeling as a function of inferred mass instead of age. The right panels show the  $[X/M]$  vs  $[M/H]$  distributions for C and N. The typical uncertainty is shown in the top right corner for C and bottom right corner for N. Stars for which the  $[X/M]$  uncertainty is larger than twice the typical uncertainty have their individual uncertainties shown.

dispersion of red giants given the hierarchically modelled SFH and a Chabrier lognormal IMF. As in F16, we assume that the metallicity distribution function is flat within the  $[M/H]$  uncertainty. The right panels of Fig. 5 show the  $[C/M]$  and  $[N/M]$  vs  $[M/H]$  distributions for the sample. Because the creation of N in the CN cycle is caused by the depletion of C, we also show the results of the hierarchical modelling for the  $[C/N]$  abundance ratio as a function of both age and mass in Fig. 6.

We find a steep increase in age and decrease in mass with increasing  $[C/M]$ , as well as a contrasting steep decrease in age and increase in mass with increasing  $[N/M]$ . The relation is also clearly seen in the  $[C/N]$  abundance ratio. This is consistent with the CN cycle and dredge-up phase having a stronger effect on higher mass, younger red giant stars. This effect has been explored both with models and empirically as a means of separating stellar populations by Masseron & Gilmore (2015) and as a more precise proxy for individual ages of red giants in the full APOGEE sample by Martig et al. (2016). The  $[C/N]$ -mass relation derived here compares very well with the relation presented by Masseron et al. (2017) using APOKASC (APOGEE + *Kepler* Asteroseismology Science Consortium) targets, which have asteroseismic mass estimates. Fig. 6 shows the sample from Masseron et al. (2017, small black dots) for comparison. Our sample has slightly lower  $[C/N]$  values, but we use calibrated DR14 values instead of externally corrected DR12 values as is done by Masseron et al. (2017). We show results from the models of Lagarde et al. (2012) in Fig. 6 with (dashed line) and without (dotted line) rotation and thermohaline mixing. The comparison of our results to the models of Lagarde et al. (2012) is consistent with that of Masseron et al. (2017), who do a similar comparison using APOKASC clump stars in the open cluster NGC 6819, see their fig. 5. Our results support the validity of the methods

of Martig et al. (2016) to use  $[C/M]$  and  $[N/M]$  abundance ratios as an age proxy for giants in the solar neighbourhood.

The massive RC stars in our sample have preferentially high  $[N/M]$ , low  $[C/M]$ , and low  $[C/N]$ . Therefore the log  $g$  overcorrection for massive RC stars discussed in §2 could be pushed the lowest  $[C/N]$  bins towards older ages and lower masses. If corrected, the mean mass of the lowest  $[C/N]$  bins would be more massive and the trend would flatten, bringing it into better agreement with both the models of Lagarde et al. (2012) and the APOKASC observations of Masseron et al. (2017).

Recent studies of solar twins in the solar neighborhood have found a trend in  $[C/Fe]$  with age such that solar twins with low  $[C/Fe]$  are younger than stars with high  $[C/Fe]$ , although with a large amount of scatter (Nissen 2015; Spina et al. 2016; Nissen et al. 2017; Bedell et al. 2018). As these solar twin stars have not undergone internal mixing like the giant branch stars, this  $[C/Fe]$ -age relation is likely to reflect Galactic evolution rather than stellar evolution. If corrected for such an underlying trend, the observed  $[C/N]$ -mass relation would come into slightly better agreement with the models. Any correction based on the solar twins would be small, up to 0.1 dex in  $[C/Fe]$ . In order to further check for possible underlying trends of C and N with age, we examine the  $[C+N/M]$ -age relation, Fig. 7. The CN cycle creates an excess of N while depleting C, but should preserve the total C+N abundance. We find that the trend with age is fairly flat with a large age dispersion for most  $[C+N/M]$  abundances. There is a weak trend such that stars with high  $[C+N/M]$  are younger than stars with low  $[C+N/M]$ . This is opposite to the  $[C/Fe]$ -age trend observed in solar twins. Unfortunately, N is almost impossible to measure in optical spectra, so no  $[N/Fe]$ -age trend has been examined for solar twins. We find that potential corrections to the CN-mass relation of giants in the solar neighborhood due to underlying



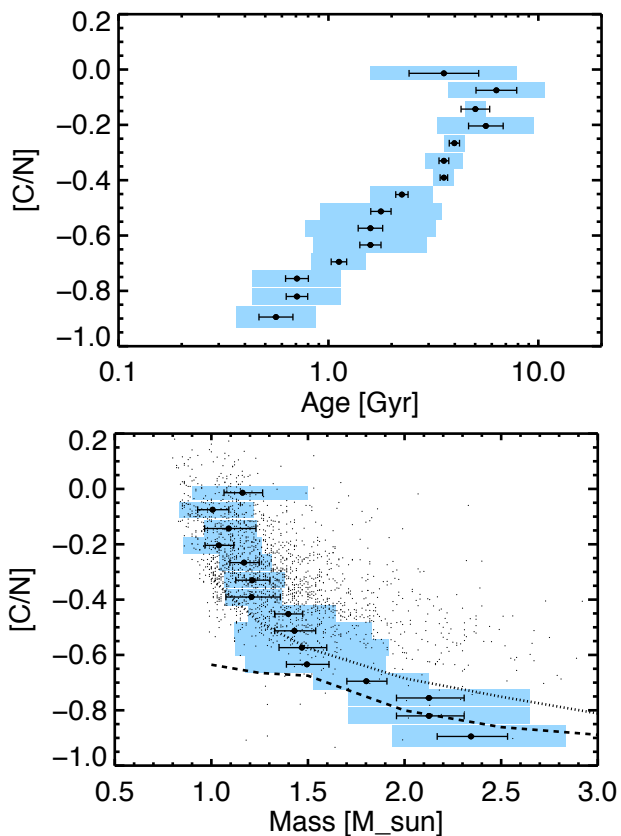


**Figure 6.** The top panel is the same as the left panels of Fig. 2 but for [C/N]. The bottom panel shows the results of the hierarchical modelling as a function of inferred mass instead of age. Theoretical models from Lagarde et al. (2012) are shown with (dashed line) and without (dotted line) rotation and thermohaline mixing. The small dots show the sample of APOKASC stars from Masseron et al. (2017)

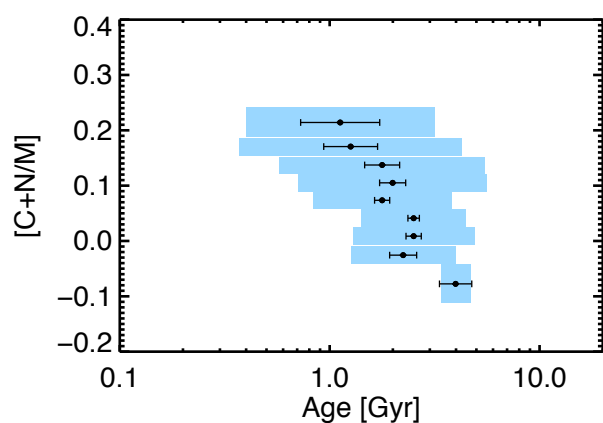


**Figure 7.** The same as for the left panel of Fig. 2 but for [C+N/M].

Galactic trends are small, but should be better characterised by looking at [N/M]-age trends in APOGEE dwarf and sub-giant stars.

Although our results confirm the close relation between [C/N] and mass/age for giants, we caution that this trend does have a mean  $\log(\text{age})$  dispersion of 0.2 dex. This sets

a lower limit of approximately 0.2 dex, depending on the CN abundance uncertainties, on the precision with which the age of a giant can be determined from its [C/N] ratio. This limit is consistent with the age uncertainty reported by Martig et al. (2016) and Ness et al. (2016). We caution that this is only a confirmation of the relation in the solar neighbourhood and may not be applicable in other regions of the Galaxy. As discussed by Martig et al. (2016), differences in the birth abundances of C and N at different Galactocentric radii could introduce false trends in the age. Recent improvements in the modelling of stellar interiors has revealed that including the thermohaline instability can have a significant effect on surface [C/N] abundances of evolved stars (see Lagarde et al. 2017), confirming the need for great care when using surface C and N abundances to interpret age trends of giant stars.

We emphasize again that the trends in Fig. 5 and 6 do not reflect Galactic chemical evolution like those in Fig. 2-4. Rather, for a star to enter our sample it must be a red giant, and its age is therefore tightly correlated with its mass. The mass in turn determines the level of carbon depletion and nitrogen enhancement in the surface abundances of giant stars as a consequence of nuclear processing and dredge up.

### 3.3 The $\alpha$ -elements

The  $\alpha$ -elements measured by APOGEE are O, Mg, Si, S, Ca, and Ti. Fig. 8 and 9 show the parameters of a model SFH constrained as a function of these  $\alpha$ -elements and the [X/M] vs. [M/H] distributions, with the typical uncertainty indicated in the top right corner of each panel. We find generally that the individual  $\alpha$ -elements increase in mean age with increasing [X/M] abundance ratio, in agreement with the overall  $[\alpha/M]$  trend from Fig. 2 and F16. The agreement with the dotted line fit to the  $\alpha$ -age relation is extremely close for O, Mg, and the higher abundance bins of Si and Ca.

*Oxygen.* We find that the mean age steeply increases with [O/M], and that [O/M] strongly increases with decreasing [M/H]. These trends are in agreement with many previous observations of dwarfs and subgiants in the solar neighbourhood (e.g. Ramírez et al. 2013; Nissen 2015; Spina et al. 2016; Adibekyan et al. 2016). The bin with [O/M]  $\approx$  0.15 is a bit of an outlier with a younger mean age and very large age dispersion compared to the overall trend. The stars in this bin also cover a large range in metallicity, though this is true for many other bins as well. As H. Jönsson et al. (2018, in preparation) discuss, the ASPCAP [O/M] abundances are lower than literature results in the metal-poor stars. The difference in [O/M] between ASPCAP and literature appears to have a [M/H] dependence, which could be caused the strong sensitivity of the OH lines to  $T_{\text{eff}}$ . The lowest [O/M] bins could be affected by the log-gover correction for massive RC stars. If corrected, these bin would be slightly younger, bringing the trend into better agreement with the  $[\alpha/M]$  line.

*Magnesium* The increase in mean age with [Mg/M] is strikingly well defined, with a smaller age dispersion at each [Mg/M] bin than is seen in  $[\alpha/M]$  and the other elements. This could be in part because of the high precision of the Mg abundance measurements, see the typical uncertainty shown in Fig. 8. A strong [Mg/M]-age relation has been observed

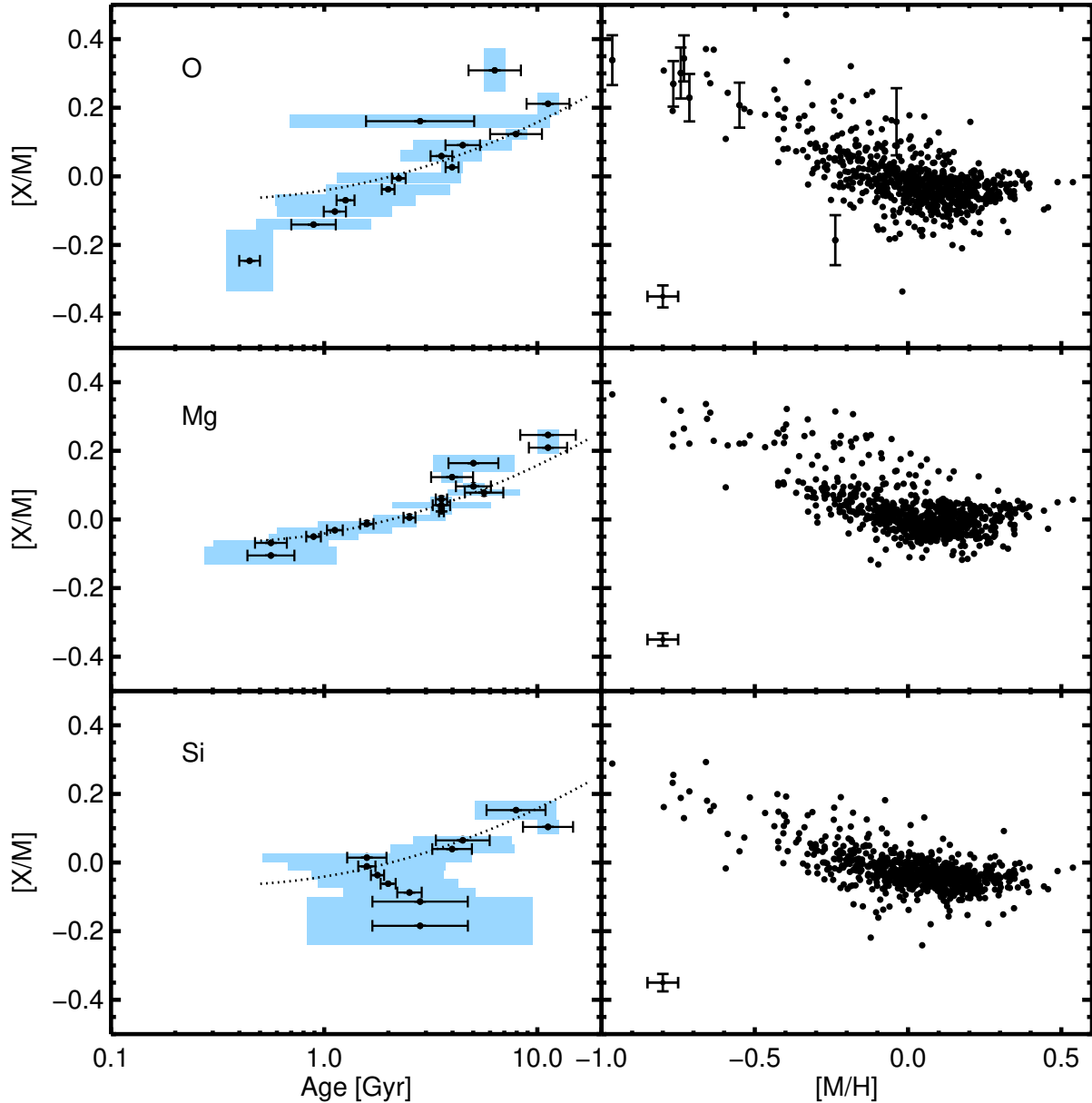


**Figure 8.** Same as Fig. 5 for models of SFH constrained as a function of  $[X/M]$  for O, Mg, and Si. As in Fig. 2, the dotted line represents the quadratic fit to the  $\alpha$ -age relation. The typical uncertainty is shown in the bottom left corner. Stars for which the  $[X/M]$  uncertainty is larger than twice the typical uncertainty have their individual uncertainties shown.

in other samples of local dwarfs (see e.g. Nissen 2015; Spina et al. 2016; Bedell et al. 2018). The tightness of the relation shown here is interesting because, as seen in Fig. 8, stars with a single  $[Mg/M]$  abundance have up to a 0.8 dex spread in  $[M/H]$ , but the age dispersion is small. This suggests a much closer relation between age and  $[Mg/M]$  than  $[M/H]$ . This is consistent with the SFH models constrained as a function of  $[M/H]$  in Fig. 3. The stars in each  $[M/H]$  bin have a range of  $[Mg/M]$  values as well as a large age dispersion. From comparisons to independent analyses and literature results, H. Jönsson et al. (2018, in preparation) conclude that Mg is the most accurately determined  $\alpha$ -element abundance in APOGEE. The lowest  $[Mg/M]$  bin could be affected by the log-govercorrection for massive RC stars. If corrected, this

bin would be slightly younger, bringing the trend into better agreement with the  $[\alpha/M]$  line.

*Silicon.* The mean age increases with increasing  $[Si/M]$  above solar, but below solar values the mean age decreases with increasing  $[Si/M]$  and has a larger age dispersion. The lower  $[Si/M]$  bins are in strong disagreement with the  $[\alpha/M]$  trend and literature results. Previous studies of solar-like stars in the solar neighbourhood have found a smooth increase in age with increasing  $[Si/Fe]$ , and specifically young ages for low  $[Si/Fe]$  stars (see e.g. Nissen 2015; Spina et al. 2016; Bedell et al. 2018). Snaith et al. (2014) find a steep and tight relation between  $[Si/Fe]$  and age for Si enhanced dwarfs in the solar neighbourhood that flattens but continues at young ages and low  $[Si/M]$ . The shape of the  $[Si/M]$  with  $[M/H]$  of our sample is consistent with the solar neigh-

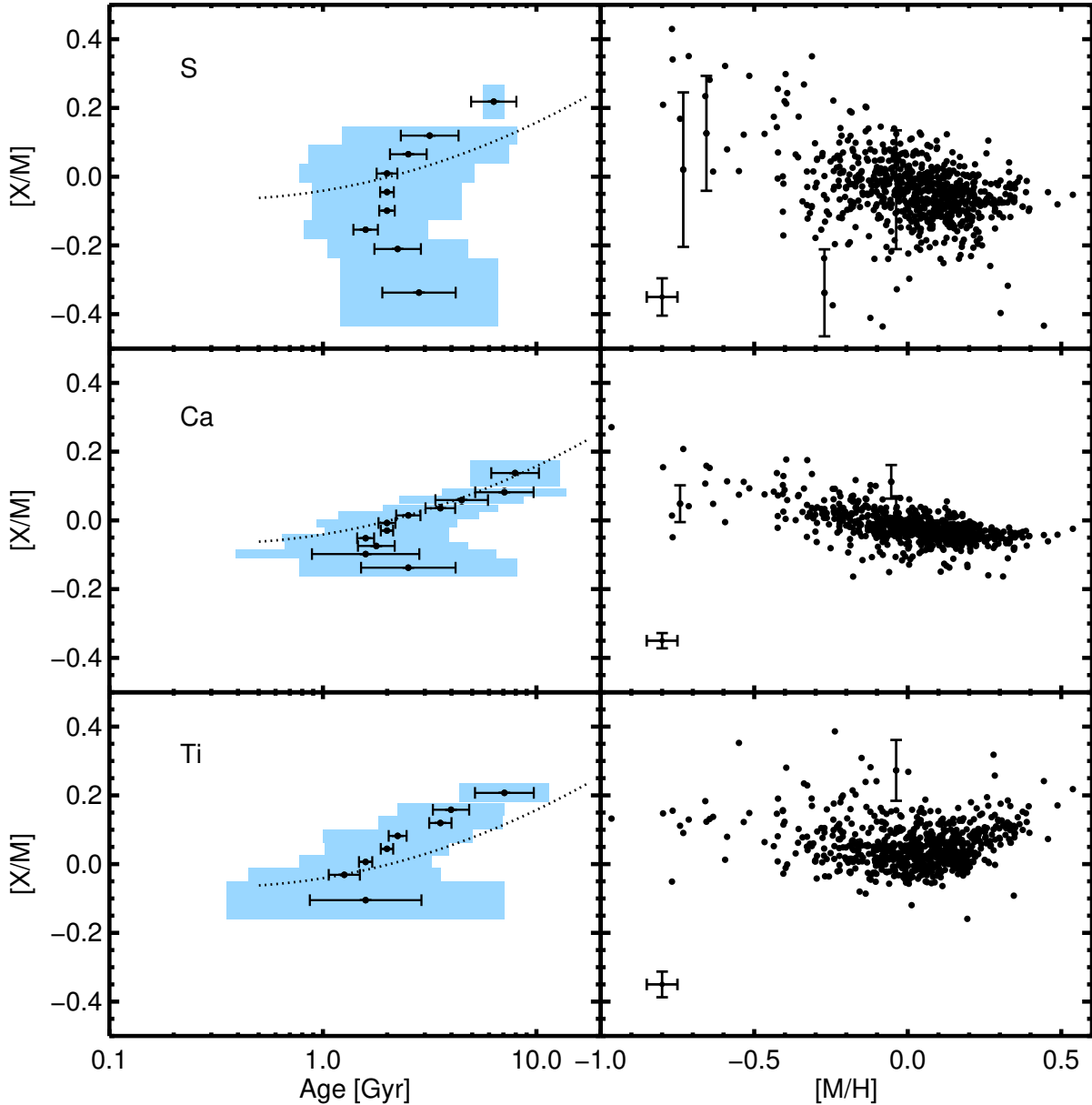


**Figure 9.** Same as Fig. 5 for models of SFH constrained as a function of  $[X/M]$  for S, Ca, and Ti. As in Fig. 2, the dotted line represents the quadratic fit to the  $\alpha$ -age relation.

bourhood sample of Bensby et al. (2014), although the values are a bit lower in APOGEE. As noted by Jönsson et al. (2018, in preparation), the APOGEE DR14  $[\text{Si}/\text{M}]$  vs  $[\text{M}/\text{H}]$  is now consistent with the analysis of Hawkins et al. (2016). Therefore, we do not find a convincing reason to distrust the APOGEE DR14 Si abundances in this sample despite the odd age trend.

*Sulphur.* We find that S behaves similarly to Si, but is consistent with a flat relation. The abundance bins are larger due to larger abundance uncertainties and the age dispersion is large at all  $[\text{S}/\text{M}]$ . Spina et al. (2016) and Adibekyan et al. (2016) both find a flat relation at lower  $[\text{S}/\text{Fe}]$  abundances and younger ages, but an increase in age for the most  $[\text{S}/\text{Fe}]$  rich stars. Nissen (2015) finds a steady increase in the age with increasing  $[\text{S}/\text{Fe}]$ , although they have no stars with the age of the most  $[\text{S}/\text{Fe}]$  rich stars of Spina et al. (2016)

and Adibekyan et al. (2016). Although there is an overall increase in the  $[\text{S}/\text{M}]$  abundance with decreasing metallicity, there is a large spread in the  $[\text{S}/\text{M}]$  vs.  $[\text{M}/\text{H}]$  distribution and the typical APOGEE uncertainty in  $[\text{S}/\text{M}]$  is larger than many of the other elements. The large  $[\text{S}/\text{M}]$  measurement uncertainties could be blurring the age trend, see Fig. 12.

*Calcium.* Ca shows an increase in mean age with increasing  $[\text{Ca}/\text{M}]$ , which steepens at higher  $[\text{Ca}/\text{M}]$  abundances. The lower  $[\text{Ca}/\text{M}]$  bins have stars with a larger spread in  $[\text{M}/\text{H}]$  and also larger age dispersions. The lowest  $[\text{Ca}/\text{M}]$  bin has an older mean age and a very large age dispersion, in the same manner as the low  $[\text{Si}/\text{M}]$  and  $[\text{S}/\text{M}]$  bins. However, as this is the lowest abundance bin, we are cautious to draw strong conclusions from this bin alone. da Silva et al. (2012) and Spina et al. (2016) find that  $[\text{Ca}/\text{Fe}]$  decreases with age for young stars, but increases

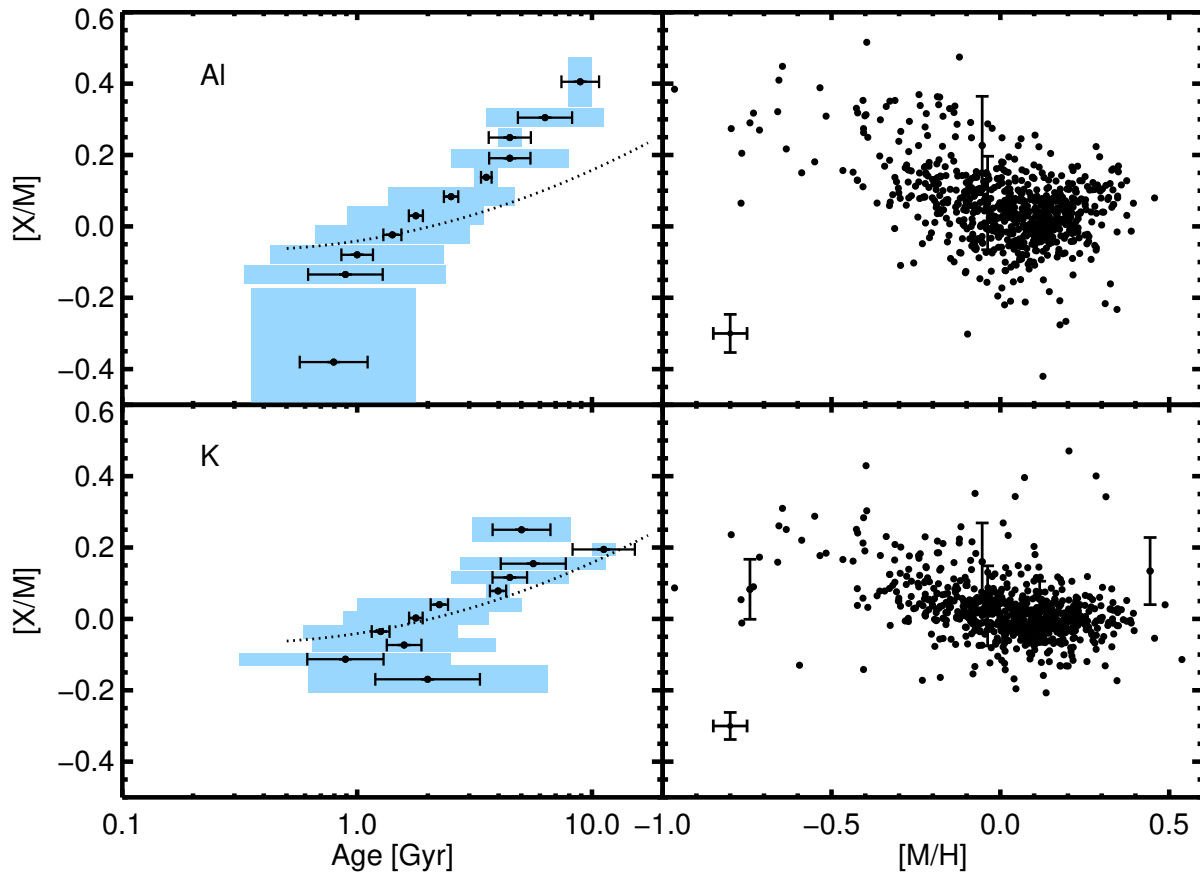


**Figure 10.** Same as Fig. 8 but for models of SFH constrained as a function of  $[X/M]$  for Al and K. As in Fig. 2, the dotted line represents the quadratic fit to the  $\alpha$ -age relation.

with age after about 5 Gyr. Our result of a steeper increase in mean age at the most Ca-enhanced bins, and perhaps a turn towards older ages in the lowest  $[Ca/M]$  bin, is consistent with these results. Nissen (2015) and Adibekyan et al. (2016) find the  $[Ca/M]$ -age relation to be fairly flat, although they do not sample a large range of  $[Ca/M]$  values.

*Titanium.* We find an increase in age with increasing  $[Ti/M]$ , similar to the  $[\alpha/M]$  trend, with slightly younger mean ages. Although there is a large age dispersion in all  $[Ti/M]$  bins, particularly the lowest bins, the trend in mean age is surprisingly smooth given the  $[Ti/M]$  vs.  $[M/H]$  distribution. As has been pointed out by Holtzman et al. (2015) and Hawkins et al. (2016), the APOGEE Ti abundances are known to have a different  $[Ti/M]$  vs  $[M/H]$  distribution than the other  $\alpha$ -elements, in disagreement with other detailed abundance studies of the Milky Way disc (see e.g. Bensby et al. 2014). Hawkins et al. (2016) find that this disagreement is driven by the use of two Ti lines in ASPCAP that are either saturated or suffer from non-LTE effects. Jönsson et al. (2018, in preparation) determine that the Ti disagreement is likely due to the use of uncalibrated instead of calibrated atmospheric parameters, particularly  $T_{\text{eff}}$ , by ASPCAP when determining elemental abundances. Despite this disagreement in  $[Ti/M]$  vs  $[M/H]$ , our age trend with  $[Ti/M]$  is consistent with previous studies (da Silva et al. 2012; Nissen 2015; Spina et al. 2016; Adibekyan et al. 2016). We do not recommend drawing strong conclusions from the Ti re-

sults given the known issues with ASPCAP Ti abundances (see Holtzman et al. 2015).

While the  $\alpha$ -elements generally increase in age with increasing  $[X/M]$  abundance ratio, Si, S, and perhaps Ca show a turn towards older ages in the lowest  $[X/M]$  bins. The stars with the lowest  $[O/M]$ ,  $[Mg/M]$ , and  $[Ti/M]$  abundance ratios are not the most metal-rich stars, showing the typical ‘banana’ shape of the low  $[\alpha/M]$  sequence. However, the stars with the lowest  $[Si/M]$ ,  $[S/M]$ , and  $[Ca/M]$  abundance ratios do not have a ‘banana’ shape, but show a decreasing or flat abundance ratio with metallicity even in the most metal-rich stars. These metal-rich stars were seen to have older ages than the solar-metallicity stars in Fig. 3. Si, S, and Ca are also theoretically expected to have larger SNIa contributions than Mg and O (e.g. Thielemann et al. 2003), which could explain their different behavior.

### 3.4 Light odd-Z elements

Fig. 10 gives the age trends and  $[X/M]$  vs.  $[M/H]$  distributions for the light odd-Z elements Al, and K. Both  $[Al/M]$  and  $[K/M]$  strongly increase in age with increasing abundance ratio. We briefly discuss the trends found for Na and P, although they are not shown because the APOGEE abundance uncertainties are too large for a meaningful examination of the age-abundance trends. A full discussion of the

effects of abundance uncertainties on the age trends is given in §3.6.

*Aluminum.* The mean age smoothly increases with increasing  $[Al/M]$ . The  $[Al/M]$ -age trend is similar to, but steeper than the  $[\alpha/M]$ -age relation line. The  $[Al/M]$  vs  $[M/H]$  distribution is similar to the  $\alpha$ -elements but with more scatter. This is consistent with the observations of Nissen (2015), Spina et al. (2016), and Bedell et al. (2018) who find that  $[Al/Fe]$  steeply increases with age. Smiljanic et al. (2016) find a shallower  $[Al/Fe]$ -age relation using GES data. Bensby et al. (2014) also find an  $\alpha$ -like behavior of  $[Al/Fe]$  with large scatter at the metal-poor end. Hawkins et al. (2016) found that some of the Al I lines are saturated or likely suffer from NLTE effects. Nordlander & Lind (2017) find that the 16750 Å Al I line is affected by departures from LTE and also from hyperfine splitting.

*Potassium.* We find that the mean age increases steadily with increasing  $[K/M]$ , very similar to the  $\alpha$ -age relation line. The  $[K/M]$  vs  $[M/H]$  distribution is also  $\alpha$ -like. The bin with the highest  $[K/M]$  abundance ratio could be strongly influenced by the metal-rich, K-enhanced stars. Like Ca, the lowest  $[K/M]$  bin has an older mean age and the stars in this bin have a 1.0 dex range in metallicity. These highest and lowest  $[K/M]$  bins contain several stars that do not lie within the main  $[K/M]$  vs  $[M/H]$  distribution. The K lines used by ASPCAP are both slightly blended. Spina et al. (2016) do present K abundances, but they do not find any correlations between age and  $[K/Fe]$ , having very large scatter in  $[K/Fe]$  at all ages.

*Sodium.* We find that the mean age slightly decreases with increasing  $[Na/M]$ , with a large age dispersion at most abundances. The  $[Na/M]$  vs  $[M/H]$  distribution is very scattered, but is generally increasing in  $[Na/M]$  with increasing  $[M/H]$ . The uncertainties in Na are large because the two Na lines available in the APOGEE spectra are very weak.

*Phosphorus.* The mean age is slightly decreasing with increasing  $[P/M]$ , with large age dispersions in all bins, similar to the behavior of  $[Na/M]$ . The  $[P/M]$  vs.  $[M/H]$  distribution appears to be generally decreasing in  $[P/M]$  with increasing metallicity, although the scatter is very large. This is opposite to the behavior of  $[Na/M]$ .

### 3.5 Fe-peak elements

The age trends and  $[X/M]$  vs  $[M/H]$  distributions for the Fe-peak elements are shown in Fig. 11. The measurement of  $[M/H]$  in ASPCAP is heavily weighted by the contributions from elements in this group. The behavior of  $[Ni/M]$  is remarkably  $\alpha$ -like, while the behavior of  $[Mn/M]$  closest matches the  $[M/H]$  trend. V and Co are not shown due to their larger abundance uncertainties.

*Vanadium.* We find that the mean age is flat with  $[V/M]$ , with a large age dispersion at all abundance bins. The  $[V/M]$  vs  $[M/H]$  distribution has large scatter with no clear trend and large uncertainties.

*Chromium.* The mean age is flat with  $[Cr/M]$  over the narrow range of  $[Cr/M]$  abundances, with a large age dispersion at all  $[Cr/M]$  bins. In this sample,  $[Cr/M]$  is flat with metallicity, in agreement with Bensby et al. (2014). There are a few high  $[Cr/M]$  stars around solar metallicity and one with very low metallicity that do not lie within the main  $[Cr/M]$  vs  $[M/H]$  distribution. These highest  $[Cr/M]$  stars

have a slightly older mean age. Recent studies of solar-like stars find  $[Cr/M]$  to be either flat or weakly decreasing with age (da Silva et al. 2012; Nissen 2015; Spina et al. 2016; Adibekyan et al. 2016; Bedell et al. 2018), which is consistent with our results.

*Manganese.* The abundance-age relation of  $[Mn/M]$  is very similar to the age-metallicity relation from Fig. 3. We find that the mean age decreases with increasing  $[Mn/M]$  until about solar  $[Mn/M]$ , then increases with increasing  $[Mn/M]$  abundance above solar  $[Mn/M]$ . The  $[Mn/M]$  vs  $[M/H]$  distribution is very tight, and smoothly increases with increasing  $[M/H]$  across all metallicities. Again, this is consistent with the most metal-rich stars being older than the solar abundance stars. This age trend is consistent with da Silva et al. (2012) who find that the highest  $[Mn/M]$  stars have intermediate ages. Spina et al. (2016) find large scatter in the  $[Mn/M]$ -age relation.

This  $[Mn/M]$  vs.  $[M/H]$  distribution is very similar to the distribution found by Battistini & Bensby (2015) without applying NLTE corrections. Battistini & Bensby (2015) find that the distribution looks quite different after applying NLTE corrections, becoming a flat distribution. This brings it into agreement with the Ni and Cr distributions. Although that analysis was done with optical lines, the strong agreement between APOGEE and the LTE distribution of Battistini & Bensby (2015) is an indication that there could be NLTE corrections needed for the  $H$ -band Mn lines used by APOGEE. However, it may also indicate that the NLTE correction for Mn is overestimated for the optical lines.

*Cobalt.* We find a large amount of scatter in the mean age of the  $[Co/M]$  bins, with no significant trend with abundance. There are also large age dispersions at all  $[Co/M]$  bins. The  $[Co/M]$  vs  $[M/H]$  distribution has a large scatter as well, with a large mean uncertainty.

*Nickel.* Although the range of  $[Ni/Fe]$  abundances is small (note the change in  $y$ -axis range for Ni in Fig. 11), the ASPCAP uncertainties are also very small. The mean age increases steeply and smoothly with increasing  $[Ni/M]$  over the narrow abundance range. The agreement with the  $\alpha$ -age line is remarkably good. The  $[Ni/M]$  vs  $[M/H]$  distribution is also very tight and looks  $\alpha$ -like but flatter. The age trend is consistent with previous studies that find an overall increase in age with increasing  $[Ni/Fe]$  abundance (e.g. Nissen 2015; Nissen et al. 2017; Spina et al. 2016; Bedell et al. 2018). However, the trend presented here is steeper than in previous work. Although the Ni trends agree with observed trends on solar twins, the strong  $\alpha$ -like behavior of Ni is not predicted by theoretical nucleosynthesis calculations (e.g. Kobayashi et al. 2006).

### 3.6 Effects of abundance uncertainties

We do note that uncertainties in the ages and elemental abundance measurements can have the effect of blurring the presence of an abundance-age relation. As a test of this effect, we created from a mock sample of 10,000 stars randomly assigned  $[X/M]$  abundances to roughly match the  $[\alpha/M]$  distribution of our observed sample, i.e. more stars with low  $[X/M]$  than with high  $[X/M]$ . We performed the same test on a sample with a uniform distribution of  $[X/M]$  and find similar results. For each star we assigned an age determined using the quadratic fit to the observed  $[\alpha/M]$ -

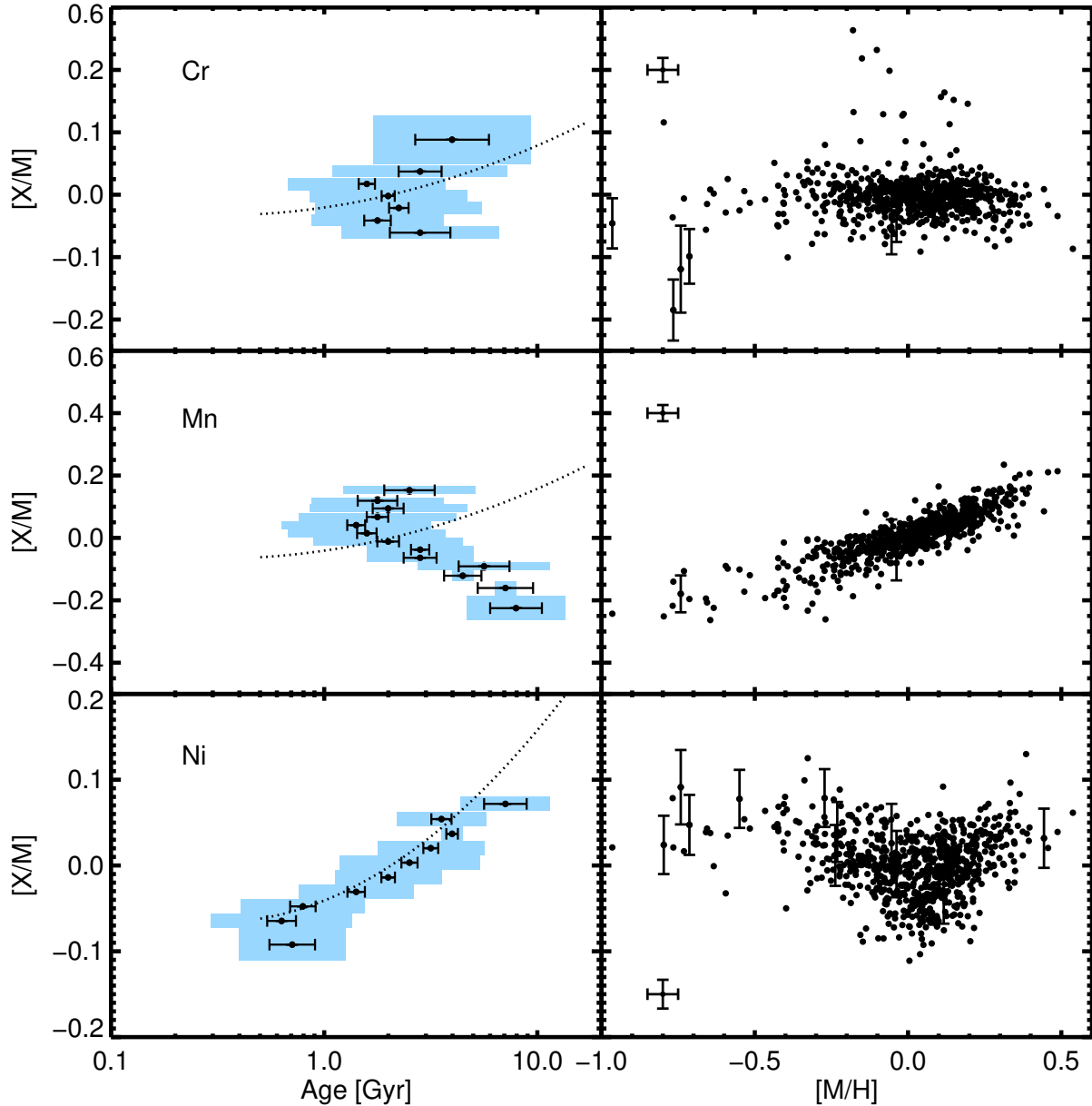


**Figure 11.** Same as Fig. 8 but for models of SFH constrained as a function of  $[X/M]$  for Cr, Mn, and Ni. As in Fig. 2, the dotted line represents the fit to the  $\alpha$ -age relation.

$\log(\text{age})$  relation, Equation 1. We then applied Gaussian noise to both the age and the  $[X/M]$  abundance with a  $\sigma$  of 0.16 dex in  $\log(\text{age})$  and increasing from 0.02 to 0.30 dex in  $[X/M]$ . In Fig. 12 the resulting abundance-age trends binned in the same way as the observed data, i.e. bin widths equal to the abundance uncertainty and containing at least 15 stars. The red points indicate the mean age of the mock stars in the bin and the error bars indicate the standard deviation. Equation 1 is also shown as the dotted line to indicate the underlying  $[X/M]$ -age relation. The  $[X/M]$  uncertainty used in each panel is given in the upper left corner.

From this test we find that an underlying abundance-age trend can be nearly completely erased if the abundance measurement errors are large enough. This could be strongly affecting our observed trends for Na, P, V, and Co, which have mean uncertainties of 0.09, 0.10, 0.07, and 0.09 dex,

respectively. From Fig. 12 it appears that any underlying abundance-age relation in these elements must be shallower than the observed  $[\alpha/M]$ -age relation to result in their respective flat relations, given the observational uncertainties. Although the abundance uncertainties could explain the flat relations seen in Na, P, V, and Co, we do not find that larger abundance errors are able to produce the reversal in the abundance-age relation at either high or low  $[X/M]$  such as that observed in Si, S, Ca, and Mn (0.03, 0.05, 0.02, and 0.03 dex uncertainty, respectively). While the  $[S/M]$ -age relation looks similar to the trends produced by very large abundance uncertainties, the reported ASPCAP uncertainty is at least 0.10 dex smaller. This suggests that either the underlying  $[S/M]$ -age relation is significantly shallower than the observed  $[\alpha/M]$ -age relation or the ASPCAP uncertainties are significantly underestimated for this element.

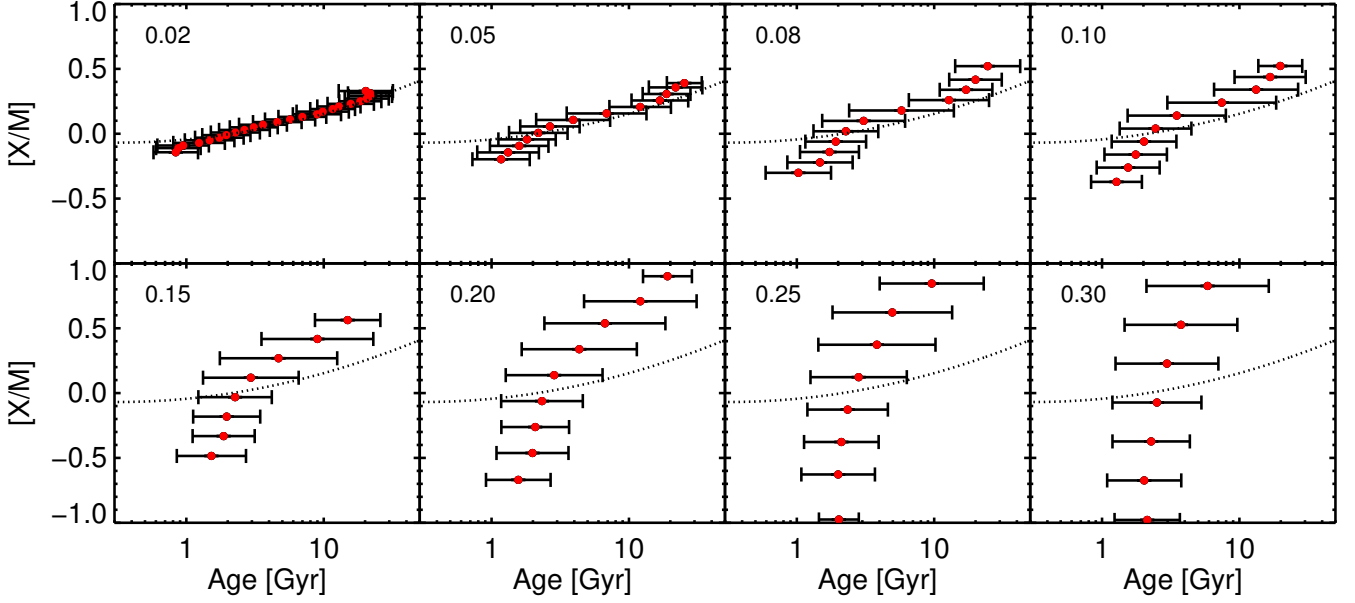


**Figure 12.** The abundance–age relations for mock data with age uncertainties of 0.16 dex and increasing abundance uncertainties from 0.02 – 0.30 dex. The red points are the mean age of the abundance bin and the error bars show the standard deviation of the mean age. The observed  $\alpha$ –age fit, Equation 1 is shown as the dotted line. The  $[X/M]$  uncertainty of each panel is shown in the upper left corner of the panel.

$[O/M]$  and  $[Mg/M]$  are consistent with the observed  $[\alpha/M]$ –age relation within their mean uncertainties of 0.03 and 0.02 dex, respectively. However, given these uncertainties, the slight age offset of the high abundance ratio bins are significant and may indicate a parallel but offset abundance–age relation for the  $\alpha$ -rich sequence. The mean uncertainties of Al and K (0.05 and 0.04 dex, respectively) suggest that the underlying abundance–age relation may be stronger than the observed relation for these elements. The observed abundance–age relations of Cr, Mn, and Ni should also be consistent with the underlying trend given the uncertainties of 0.04, 0.03, and 0.02, respectively. However, it should be noted that we have only tested the effects of the abundance uncertainties assuming an  $\alpha$ -like age relation. While we did confirm that both a shallower age relation and larger age uncertainties also could not produce the  $[M/H]$ -like age relation, we did not have a robust  $[M/H]$ –age relation unaffected by possible migration with which to test the Fe-peak elements.

Through examining the abundance–age trends of the individual elements, we highlight that the differences between individual elements can be a tool used to disentangle the complicated processes of Galactic evolution. For example, we find surprisingly large variations in the abundance–age trends even among the  $\alpha$ -elements that cannot be explained by the age or abundance uncertainties alone.

#### 4 GALACTIC CHEMICAL EVOLUTION MODELS

A key goal of deriving age measurements and detailed chemical abundance observations is to place constraints on models of Galactic and chemical evolution. In this section we com-

pare our observations to the predictions of two relatively simple GCE frameworks, one analytic and one numerical. The successes and failures of these models are both informative.

##### 4.1 One-Zone Models and Mixtures

We first discuss our results in the context of simple one-zone chemical evolution models and mixtures of such models that could represent the impact of radial mixing on a disc whose evolutionary parameters vary with Galactocentric radius. For this discussion we draw on analytic results from Weinberg, Andrews & Freudenberg (2017, hereafter WAF17). Our goal is not to derive a model that reproduces all aspects of the data but rather to understand how physical parameters affect the abundance–age relations and explore qualitative implications of the APOGEE measurements for disc history.

The key parameters of the WAF17 analytic solutions are the IMF-averaged supernova yields for core collapse supernovae (CCSN) and Type Ia supernovae (SNIa), the star formation efficiency time-scale  $\tau_* \equiv M_{\text{gas}}/\dot{M}_*$ , the outflow mass-loading factor  $\eta \equiv \dot{M}_{\text{out}}/\dot{M}_*$ , and a time-scale for the star formation history  $\tau_{\text{sFH}}$ . The analytic solutions assume metallicity-independent yields and a star formation history (SFH) that is exponential,  $\dot{M}_*(t) \propto e^{-t/\tau_{\text{sFH}}}$ , linear-exponential,  $\dot{M}_*(t) \propto te^{-t/\tau_{\text{sFH}}}$ , constant, or a linear combination of these forms. CCSN are assumed to return newly produced oxygen and iron to the ISM instantaneously at a rate  $m_{\text{O}}^{\text{CC}}\dot{M}_*$  and  $m_{\text{Fe}}^{\text{CC}}\dot{M}_*$ , respectively, while SNIa return iron at a rate  $m_{\text{Fe}}^{\text{Ia}}\dot{M}_*$  with exponential delay time distributions (DTD). For the calculations here we use a sum of two exponentials that approximates a  $t^{-1.1}$  power-law DTD (Maoz, Mannucci & Brandt 2012) with a minimum delay time of

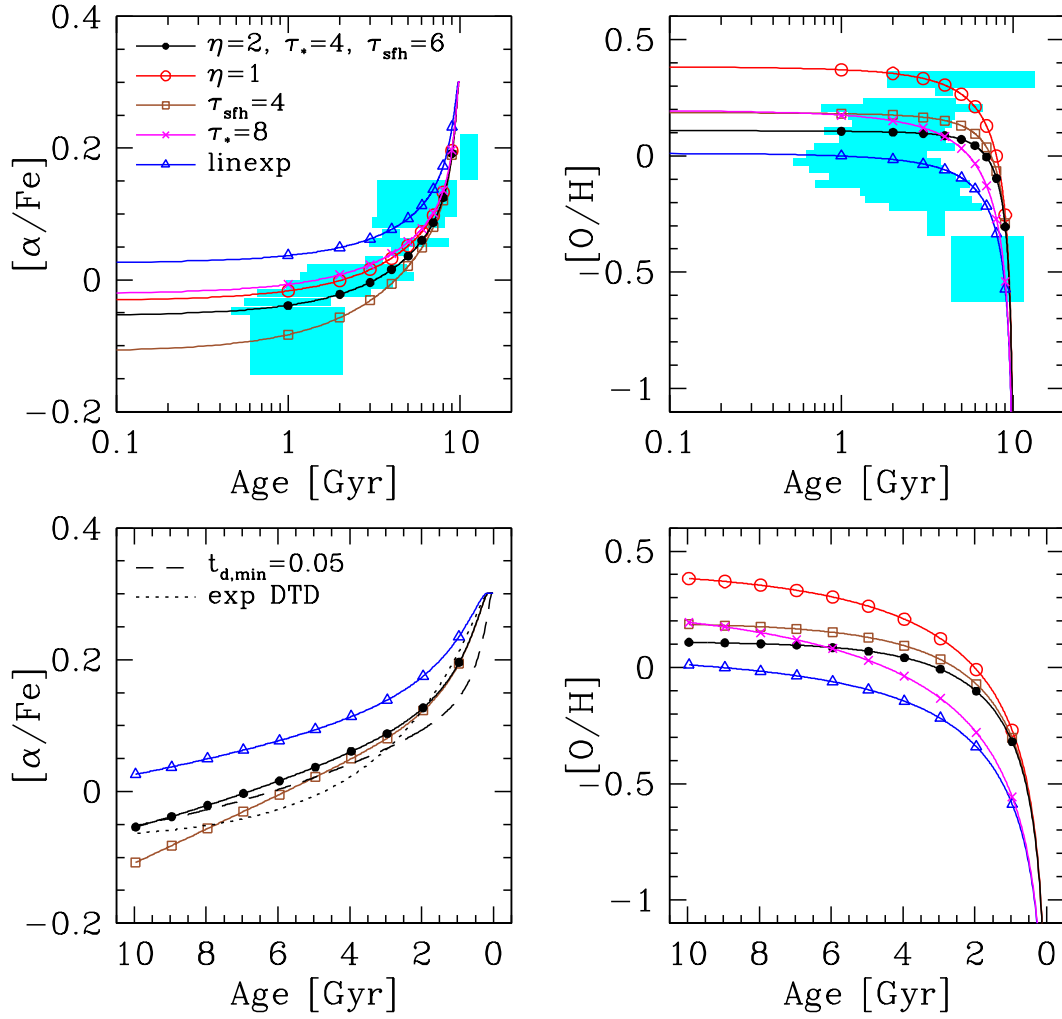


**Figure 13.** Evolutionary tracks of  $[\alpha/\text{Fe}]$  (left) and  $[\text{O}/\text{H}]$  (right) for five one-zone models. In the upper panels cyan rectangles represent the observational measurements from Fig. 2 and 3. The black curves represents a model with  $\eta = 2$ ,  $\tau_* = 4$  Gyr,  $\tau_{\text{sfr}} = 6$  Gyr and an exponential SFR. Filled circles mark abundances at 1 Gyr intervals. Other curves show single-parameter variations away from this reference model: a lower outflow mass-loading factor ( $\eta = 1$ , red curve, open circles), a more rapidly declining SFH ( $\tau_{\text{sfr}} = 4$  Gyr, sienna curve, squares), a lower star formation efficiency ( $\tau_* = 8$  Gyr, magenta curve, crosses), or a linear–exponential SFH with the same parameter values (blue curve, triangles). Solid curves in the lower panels show the same models with a linear instead of logarithmic age axis. In the lower left panel, two models have been omitted and replaced with two variants of the central model, which have a minimum SNIa delay time of 0.05 Gyr instead of 0.15 Gyr (dashed line) or a single-exponential DTD (dotted line).

0.15 Gyr (see WAF17 for details). Stars also instantaneously recycle a fraction  $r$  of the gas and metals they are born with; we adopt  $r = 0.4$ , which is a good approximation for a Kroupa (2001) IMF. In the absence of infall, the combination of star formation and outflow would deplete the gas on an  $e$ -folding time-scale

$$\tau_{\text{dep}} = \frac{\tau_*}{1 + \eta - r}. \quad (2)$$

For an exponentially declining SFH, the evolution equation for the ISM oxygen mass fraction  $Z_{\text{O}}$  is

$$Z_{\text{O}}(t) = Z_{\text{O,eq}} \left( 1 - e^{-t/\bar{\tau}} \right), \quad (3)$$

where the equilibrium abundance is

$$Z_{\text{O,eq}} = \frac{m_{\text{O}}^{\text{cc}}}{1 + \eta - r} \times \left( 1 - \tau_{\text{dep}}/\tau_{\text{sfr}} \right)^{-1} \quad (4)$$

and the evolution time-scale is

$$\bar{\tau} = \left( \tau_{\text{dep}}^{-1} - \tau_{\text{sfr}}^{-1} \right)^{-1} = \tau_{\text{dep}} \times \left( 1 - \tau_{\text{dep}}/\tau_{\text{sfr}} \right)^{-1}. \quad (5)$$

For a linear–exponential SFH, the equilibrium abundance and time-scale  $\bar{\tau}$  are the same, but the functional form of the solution yields a slower approach to equilibrium,

$$Z_{\text{O}}(t) = Z_{\text{O,eq}} \left[ 1 - \frac{\bar{\tau}}{t} \left( 1 - e^{-t/\bar{\tau}} \right) \right]. \quad (6)$$

With an appropriate substitution for  $m_{\text{O}}^{\text{cc}}$ , these solutions describe the CCSN contribution to any element with a metallicity-independent yield. We adopt oxygen as our representative  $\alpha$ -element and identify  $[\text{O}/\text{H}]$  with  $[\alpha/\text{Fe}]$ . Analytic solutions for the SNIa iron contribution can be found in WAF17.

The gas infall rate is determined implicitly by the assumed star formation efficiency and SFH (WAF17, eq. 9).



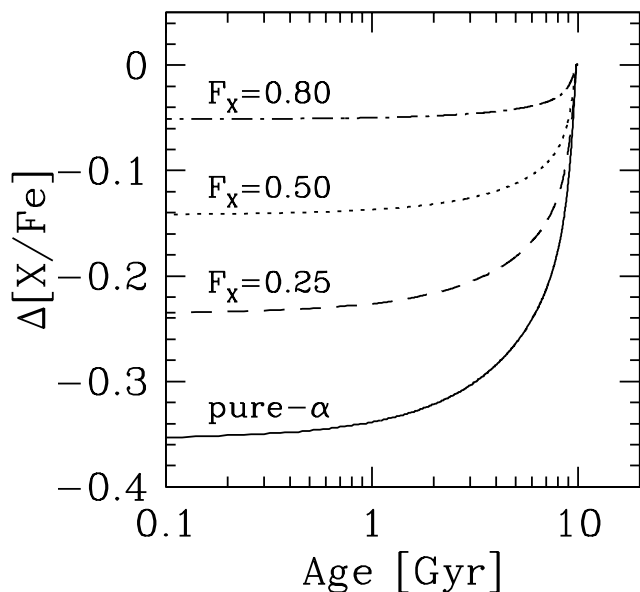


**Figure 14.** Predicted evolutionary tracks for elements with different ratios of SNIa to CCSN contribution, but metallicity-independent yields, in a one-zone model with the parameters of the black curve in Fig. 13 ( $\eta = 2$ ,  $\tau_* = 4$ ,  $\tau_{\text{sfn}} = 6$ ).  $\Delta[X/\text{Fe}]$  is the change in  $[X/\text{Fe}]$  relative to the plateau value implied by CCSN yields.  $F_X$  is the SNIa contribution relative to that of iron (see eq. 9), so a “pure- $\alpha$ ” element corresponds to  $F_X = 0$ .

For an exponential SFH one can easily show that

$$(1 - \tau_{\text{dep}}/\tau_{\text{sfn}}) = \frac{\dot{M}_{\text{inf}}}{M_{\text{gas}}/\tau_{\text{dep}}}, \quad (7)$$

so the second factor in equations (4) and (5) approaches unity if the infall rate is sufficient to replenish the ISM at the rate it is being depleted. For a gas-starved system with  $\dot{M}_{\text{inf}} \ll M_{\text{gas}}/\tau_{\text{dep}}$ , the equilibrium abundance diverges and the time-scale for reaching it also diverges; evolution in this case approaches the traditional “closed box” or “leaky box” analytic models. Conversely, the limit  $\tau_{\text{sfn}} \rightarrow \infty$  corresponds to constant SFR, with infall keeping the gas supply constant and  $(1 - \tau_{\text{dep}}/\tau_{\text{sfn}}) = 1$ .

Fig. 13 shows the evolutionary tracks of five one-zone models in the  $[\alpha/\text{Fe}]$ - $\log(\text{age})$  plane and the  $[\text{O}/\text{H}]$ - $\log(\text{age})$  plane. For oxygen and iron yields we adopt  $m_{\text{O}}^{\text{cc}} = 0.014$ ,  $m_{\text{Fe}}^{\text{cc}} = 0.0015$ ,  $m_{\text{Fe}}^{\text{la}} = 0.0015$ , based approximately on Andrews et al. (2017) but adjusted slightly to better fit the  $[\alpha/\text{Fe}] - [\text{Fe}/\text{H}]$  tracks measured by APOGEE. All models run for 10 Gyr, and points along the model curves mark abundances at 1 Gyr intervals. One can see at a glance that most of these models approximately reproduce the observed  $[\alpha/\text{Fe}]$ - $\log(\text{age})$  trend and none of them reproduces the observed  $[\text{O}/\text{H}]$ - $\log(\text{age})$  trend. The black curve shows a reference model with  $\eta = 2$ ,  $\tau_* = 4$  Gyr, and an exponential SFH with  $\tau_{\text{sfn}} = 6$  Gyr. These values are plausible choices for the solar annulus and yield approximately solar abundances at late times. Lowering  $\eta$  to one (red curve) raises the equilibrium  $[\text{O}/\text{H}]$  (eq. 4) and shifts the  $[\alpha/\text{Fe}]$  equilibrium slightly upward. Reducing  $\tau_{\text{sfn}}$  to 4 Gyr (sienna curve) raises the equilibrium  $[\text{O}/\text{H}]$  slightly, and it lowers the  $[\alpha/\text{Fe}]$  track because more rapidly declining star formation makes the ratio of delayed SNIa to instantaneous CCSN higher at any

given time. Doubling the SFE time-scale to  $\tau_* = 8$  Gyr (magenta curve) slows the approach to equilibrium by increasing  $\tau_{\text{dep}}$ , with a small shift in the equilibrium abundance. Keeping  $\tau_* = 4$  Gyr while changing from exponential to linear-exponential SFH has a stronger impact (blue curve) because of the much slower approach to equilibrium (eq. 6).

The lower panels of Fig. 13 change the  $x$ -axis from logarithmic to linear. In this representation, it is more evident that some models still have gently rising  $[\text{O}/\text{H}]$  at  $t = 10$  Gyr, and that  $[\alpha/\text{Fe}]$  is still declining at late times in all models because of the long tail of the  $t^{-1.1}$  DTD for SNIa. The dotted black curve shows the effect of changing to a single-exponential DTD with  $\tau_{\text{la}} = 1.5$  Gyr, the form used for most of the calculations in WAF17 and Andrews et al. (2017). With fewer SNIa at long delay times, this model settles to an equilibrium  $[\alpha/\text{Fe}]$  by  $t \approx 6$  Gyr. The dashed black curve shows the effect of changing the minimum SNIa delay time from 0.15 Gyr to 0.05 Gyr while retaining the  $t^{-1.1}$  form. Here  $[\alpha/\text{Fe}]$  declines more rapidly at early times but has similar late-time behavior; in an  $[\alpha/\text{Fe}]$ - $\log(\text{age})$  plot the impact of this change is small. Changes in the SNIa yield or DTD have no impact on the  $[\text{O}/\text{H}]$ -time relation, which is the reason we have chosen to focus on modeling this relation rather than  $[\text{Fe}/\text{H}]$  vs. time.

The WAF17 analytic solutions require metallicity-independent yields, but they can be adapted to elements with different relative contributions of CCSN and SNIa. To express the behaviour in general terms, it is useful to define

$$\Delta[\text{O}/\text{Fe}] = -\log_{10} \left[ 1 + Z_{\text{Fe}}^{\text{la}}(t)/Z_{\text{Fe}}^{\text{cc}}(t) \right], \quad (8)$$

the change in  $[\text{O}/\text{Fe}]$  relative to the plateau value at early times, when CCSN dominate the enrichment for both O and Fe. Here  $Z_{\text{Fe}}^{\text{la}}(t)$  and  $Z_{\text{Fe}}^{\text{cc}}(t)$  represent the ISM iron mass fraction contributed by SNIa and CCSN, respectively, at time  $t$ . Define

$$F_X = \frac{m_X^{\text{la}}/m_X^{\text{cc}}}{m_{\text{Fe}}^{\text{la}}/m_{\text{Fe}}^{\text{cc}}}, \quad (9)$$

where  $m_X^{\text{la}}$  and  $m_X^{\text{cc}}$  are the IMF-averaged yield of element X from SNIa and CCSN. For a “pure- $\alpha$ ” element produced entirely by CCSN,  $F_X = 0$ , and for iron  $F_X = 1$ . Using Equation 8 and equation 109 of WAF17, one can show that

$$\Delta[X/\text{Fe}] = \Delta[\text{O}/\text{Fe}] + \log_{10} \left[ 1 + F_X \left( 10^{-\Delta[\text{O}/\text{Fe}]} - 1 \right) \right]. \quad (10)$$

Equation 10 can be used to convert a  $\Delta[\alpha/\text{Fe}]$ -age relation into a  $\Delta[X/\text{Fe}]$ -age relation for other elements.

Fig. 14 shows  $\Delta[X/\text{Fe}]$ -age predictions for several choices of  $F_X$ , using the parameters of the fiducial (black curve) one-zone model from Fig. 13. For reference, the yield calculations of Andrews et al. (2017) imply  $F_X = 0.24$  and 0.36 for Si and S, respectively, given the values  $m_{\text{Fe}}^{\text{la}} = m_{\text{Fe}}^{\text{cc}} = 0.0015$  that we are using here. Roughly speaking, the  $\Delta[X/\text{Fe}]$ -age relation for an element with  $F_X = 0.25$  (0.50) resembles the  $\Delta[\alpha/\text{Fe}]$ -age relation with the vertical drop scaled by a factor of 0.67 (0.39). The normalisation of an  $[X/\text{Fe}]$ -age relation further depends on the value of  $m_X^{\text{cc}}/m_{\text{Fe}}^{\text{cc}}$  relative to the solar X/Fe ratio. The observed  $[X/M]$ -age relations for Si, S, Ca, and Ti do not obviously show the trend predicted by Fig. 14 for steadily increasing  $F_X$ , and this discussion does not explain the slight increase of mean age seen for the lowest bins of

$R$ (kpc)	$\eta$	$\tau_*$	$\tau_{\text{sfr}}$	$t_{\text{start}}$
3-5	1.0	1.5	3.0	0 Gyr
5-7	1.5	2.0	3.0	2 Gyr
7-9	2.5	3.0	4.0	2 Gyr
9-11	4.0	4.0	6.0	2 Gyr
11-13	6.0	8.0	12.0	2 Gyr

**Table 1.** Mixture Model Parameters: All models adopt a linear–exponential SFH, IMF-averaged yields  $m_{\text{O}}^{\text{cc}} = 0.014$ ,  $m_{\text{Fe}}^{\text{cc}} = m_{\text{Fe}}^{\text{ia}} = 0.0015$ , and a two-exponential DTD for SNIa that approximates a  $t^{-1.1}$  power-law with minimum delay time of 0.15 Gyr (see WAF17). Units of  $\tau_*$ ,  $\tau_{\text{sfr}}$ , and  $t_{\text{start}}$  are Gyr.

Si/M, Ca/M, and Ti/M. The observed [Ni/M]-age trend, on the other hand, looks roughly like the model prediction for  $F_X \approx 0.35$ . Again, this is not consistent with theoretical predictions of SN yields and suggests the nucleosynthesis of Ni is not well understood.

All of these simple models predict one-to-one age-abundance relations and a monotonically increasing [O/H]. To better reproduce the observed distributions, we consider a more realistic model in which inflow, outflow, SFE, and SFH parameters vary with Galactocentric radius and radial migration mixes stars born at smaller and larger radii into the solar neighbourhood. One can view this mixture model as a simplified and parameterized representation of the behavior in more sophisticated models such as Schönrich & Binney (2009) and Minchev et al. (2013). Our choice of parameters for the five Galactic annuli is given in Table 1, and the  $[\alpha/\text{Fe}] - [\text{O}/\text{H}]$  evolutionary tracks of these models appear in the lower left panel of Fig. 15. We have chosen linear–exponential SFHs for these models both because we consider them more realistic than exponentials and because the slower approach to equilibrium helps reproduce the observed behavior. The inner annulus evolves from  $t = 0$  to  $t = 12$  Gyr, while the other models start at  $t = 2$  Gyr. An earlier commencement of star formation in the inner Galaxy is physically reasonable, and we find it difficult to reproduce the observed ages of the most metal-rich stars without giving the inner annulus a head start. From the inner to outer Galaxy, we increase  $\eta$  to produce a negative metallicity gradient, decrease the star formation efficiency to represent the impact of lower gas surface density, and increase  $\tau_{\text{sfr}}$  to produce more extended star formation.

The expected level of radial migration is difficult to predict from first principles because it is sensitive to properties such as disc velocity dispersion and gas fraction, bar strength, and satellite perturbations (see, e.g., Roškar et al. 2008; Bird, Kazantzidis & Weinberg 2012; Minchev et al. 2013), whose Galactic history is largely unknown. Here we adopt a simplified model of radial migration in which the stars formed in annulus  $i$  at time  $t_{\text{form}}$  are distributed in radius  $R$  at the final epoch  $t_0 = 12$  Gyr with a Gaussian distribution  $p(R) = (2\pi\sigma^2)^{-1/2} \exp[-(R - R_i)^2/2\sigma^2]$  where  $R_i$  is the central radius of the annulus and the dispersion is

$$\sigma = \sigma_0 (1 - t_{\text{form}}/t_0)^{1/2}, \quad (11)$$

growing  $\propto (\Delta t)^{1/2}$  as expected for a diffusion process. We adopt  $\sigma_0 = 2.5$  kpc for all five annuli. We also account for the exponential surface density profile of the disk by normalizing the star formation history of each annulus to produce a time-

integrated stellar mass proportional to  $e^{-R_i/R_H}$  with  $R_H = 2.5$  kpc. Thus, the number of stars of age  $t - t_{\text{form}}$  at the solar radius  $R_{\text{sol}} = 8$  kpc from annulus  $i$  is proportional to

$$F_{\text{sol}}(R_i, t_{\text{form}}) = \text{SFR}(R_i, t_{\text{form}}) e^{-(R_i - R_{\text{sol}})/R_H} e^{-(R_i - R_{\text{sol}})^2/2\sigma^2}. \quad (12)$$

This model crudely reproduces the kind of pattern seen in the disk galaxy simulations of Bird et al. (2013, fig. 15) or Minchev et al. (2013, fig. 3), in which young stars in the solar neighbourhood formed near  $R_{\text{sol}}$  but older stars come largely from the inner galaxy. The lower right panel of Fig. 15 shows the histogram of [O/H] at the solar annulus at  $t = 12$  Gyr, and the contributions from each annulus to this MDF. The metal-rich tail is dominated by stars from the  $R_i = 4$  kpc annulus, while the core of the MDF is dominated by stars from the  $R_i = 6$  kpc and  $R_i = 8$  kpc annuli. The contribution of the  $R_i = 10$  kpc annulus is small because of the exponential surface density factor, and that of the  $R_i = 12$  kpc annulus is negligible because of both the surface density factor and the small fraction of stars that migrate 4 kpc.

The principal results of the mixture model are shown by the points and range bars in the upper panels of Fig. 15, which mark the median age and the 16–84 per cent range of ages from the population mixture computed in bins of 0.04 dex in  $[\alpha/\text{Fe}]$  or 0.05 dex in [O/H]. After assigning stars to bins, we apply a 3-cell boxcar smoothing along the  $[\alpha/\text{Fe}]$  and [O/H] dimensions before computing these statistics. This convolution mitigates the artificial discreteness of our five-zone mixture, which would in practice be smoothed by observational errors, by continuous gradients, and by scatter about idealised evolutionary tracks. The mixture model is reasonably successful in reproducing the observed  $[\alpha/\text{Fe}] - \log(\text{age})$  trend and the scatter in age at a fixed  $[\alpha/\text{Fe}]$ . It does not reproduce the large age spread at  $[\alpha/\text{Fe}] \approx +0.12$ . The discrepancy in these bins could indicate that some young  $\alpha$ -enhanced stars are produced by a mechanism not represented in this model, or that some of the apparently young stars are “rejuvenated” products of binary stellar mergers (Tayar et al. 2015; Jofré et al. 2016), or that other age-determination errors have artificially broadened the age range.

The mixture model reproduces the observed [O/H]- $\log(\text{age})$  trend better than an individual one-zone model, but the match is still rather poor. From the individual zone evolutionary tracks and MDF contributions one can see the basic structure of the model. For [O/H] < 0 the population is dominated by stars formed in the solar annulus, and the age trend follows that of the  $R_i = 8$  kpc model. Just above [O/H] = 0 the dominant population shifts to stars formed in the  $R_i = 6$  kpc annulus, which are older at a given [O/H]. A similar transition to the  $R_i = 4$  kpc annulus, and another, smaller jump of median age, occurs at [O/H]  $\approx +0.2$ . The model successfully produces a large age spread near solar metallicity and an increase of median age at super-solar metallicity. However, despite the model’s adjustable parameters, we have not found a mixture that produces a median age as young as 2 Gyr at solar metallicity or the smooth increase of age with increasing [O/H] at super-solar metallicity. The model as implemented here does not take account of the vertical distribution of stars, in particular the observed trend that older stellar populations have larger

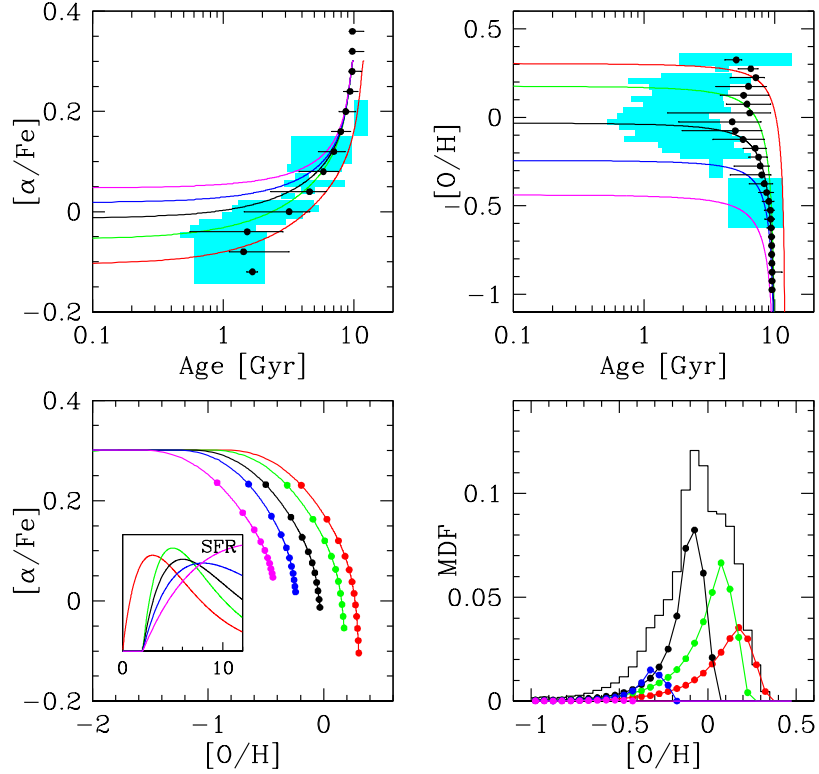


**Figure 15.** Mixture model of the age-abundance distributions. In the lower left panel, curves show the  $[\alpha/\text{Fe}] - [\text{O}/\text{H}]$  evolution of five one-zone models with the parameters given in Table 1, with points marking 1 Gyr intervals and inset panel showing the star formation histories. In the upper panels, points show the median age of stars in 0.04 dex bins of  $[\alpha/\text{Fe}]$  (left) or 0.05 dex bins of  $[\text{O}/\text{H}]$  (right), and line segments mark the 16 per cent–84 per cent range of ages in the bin. Cyan rectangles represent the APOGEE measurements. The individual model evolutionary curves are shown in the upper panels for reference. In the lower right panel, the black histogram shows the  $[\text{O}/\text{H}]$  MDF of the solar annulus at  $t = 12$  Gyr and colored lines show the contributions of individual annuli to this MDF.

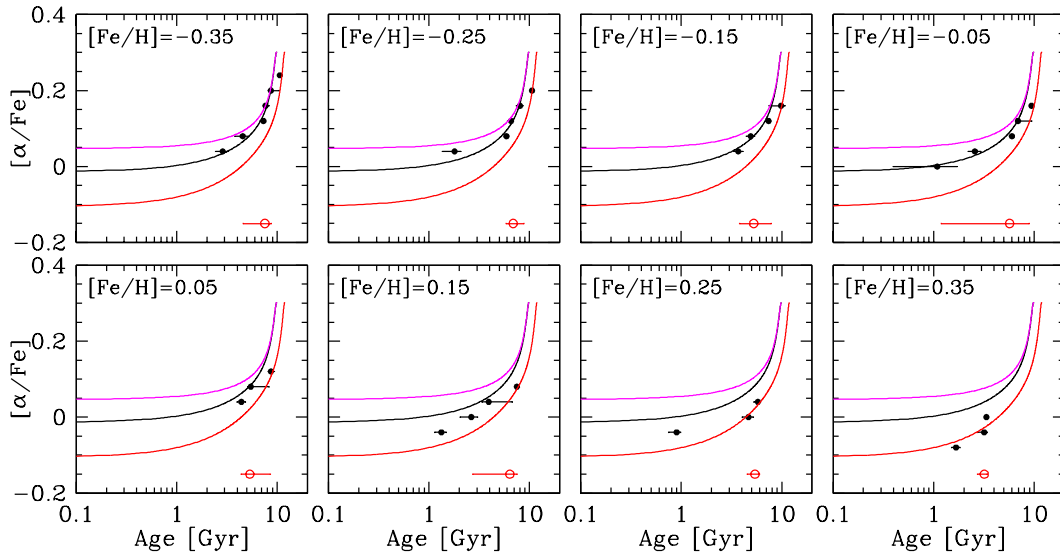


**Figure 16.**  $[\alpha/\text{Fe}]$ -age relation predicted by the mixture model in 0.1 dex bins of  $[\text{Fe}/\text{H}]$ , for comparison to Fig. 4. In each panel, filled circles and horizontal bars show the median and 16–84 per cent range of age in 0.04 dex bins of  $[\alpha/\text{Fe}]$ , while the open circle and horizontal bar represent the median age and 16–84 per cent range for the full  $[\text{Fe}/\text{H}]$  bin. Curves show the central model and the inner and outermost models contributing to the mixture, for reference. In contrast to Fig. 15, we do not include boxcar smoothing of the abundance distributions prior to computing age ranges.

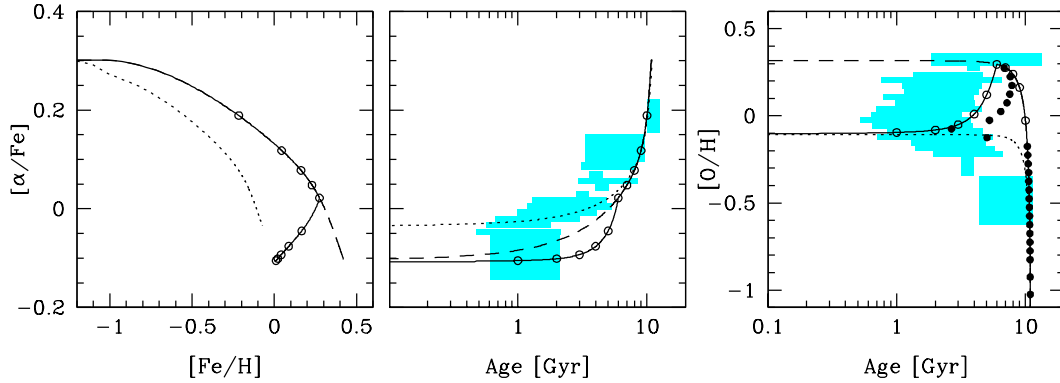


**Figure 17.** A one-zone model with a discontinuous change of parameters, from  $(\eta, \tau_*, \tau_{\text{sfn}}) = (1.0, 2.0, 5.0)$  for  $t \leq 5$  Gyr to  $(\eta, \tau_*, \tau_{\text{sfn}}) = (3.0, 4.0, 10.0)$  for  $5 < t \leq 11$  Gyr. In each panel, the solid curve shows the model evolutionary track with open circles at 1 Gyr intervals. In the right panel, filled circles show the mean age of stars in 0.05 dex bins of  $[\text{O}/\text{H}]$ . Cyan rectangles in the middle and right panels show the APOGEE measurements. In all panels, dashed and dotted curves show the tracks predicted by the first and second models, respectively, if they are run over 11 Gyr without parameter changes.

vertical scale heights. Incorporating this effect together with the local neighbourhood selection of our observational sample might lead to a younger predicted age at solar metallicity, since the older stars of the *in situ* zone would be less likely to be included in the sample.

Fig. 16 shows the predicted  $[\alpha/\text{Fe}]$ -age relation in 0.1 dex bins of  $[\text{Fe}/\text{H}]$ , similar to Fig. 4. For simplicity of interpretation, we have omitted the boxcar smoothing of abundance distributions used for the predictions in Fig. 15. In agreement with the observations, each individual  $[\text{Fe}/\text{H}]$  bin shows an  $[\alpha/\text{Fe}]$ -age relation similar to the global relation, and from inspection of Fig. 15 it is easy to see why. First, the  $[\alpha/\text{Fe}]$ -age relations of the individual models composing the mixture are similar to begin with, differing mainly in the asymptotic value at low age. Second, in any given  $[\text{Fe}/\text{H}]$  bin, the populations of one or two zones dominate, and the  $[\alpha/\text{Fe}]$ -age relation for the bin tracks the one-to-one relation of the dominant zones. The mixture model predicts very small scatter in the  $[\alpha/\text{Fe}]$ -age relation within  $[\text{Fe}/\text{H}]$  bins. The observations show substantially larger age dispersion, implying an additional source of scatter in the age-abundance relations beyond simple mixing of individually smooth one-zone models.

WAF17 note that even a one-zone model can exhibit non-monotonic metallicity evolution if the outflow mass-loading increases at late times (e.g., as a consequence of decreasing gas surface density). Fig. 17 shows an example of such a model using the 2-phase analytic solution described in §4.2 of WAF17. For  $t \leq 5$  Gyr the model has an exponential SFH with  $\eta = 1.0$ ,  $\tau_* = 2$  Gyr,  $\tau_{\text{sfn}} = 5$  Gyr and evolves to  $[\text{O}/\text{H}] \approx +0.3$ ,  $[\alpha/\text{Fe}] \approx 0$ . At  $t = 5$  Gyr the model parameters change discontinuously to  $\eta = 3.0$ ,  $\tau_* = 4$  Gyr,  $\tau_{\text{sfn}} = 10$  Gyr, with a lower equilibrium  $[\text{O}/\text{H}]$ . The continuing downward evolution of  $[\alpha/\text{Fe}]$  is driven by SNIa from stars that form before 5 Gyr but explode and deposit their iron after 5 Gyr. While the evolution of  $[\alpha/\text{Fe}]$  is monotonic, the age- $[\text{O}/\text{H}]$  relation is double valued for  $[\text{O}/\text{H}] > -0.1$ . Filled circles in the right panel show the mass-weighted mean stellar age. Clearly this model is not a good fit to the data, but it illustrates an alternative mechanism for producing young mean ages near solar metallicity and a smooth increase of age at higher metallicity. An outflow mass-loading that grows at

late times is physically plausible, and a combination of this mechanism with radial migration might be important for reproducing the full structure of the observed age-abundance relation.

Part of the difficulty in reproducing the young age at solar metallicity in the mixture model of Fig. 15 is that each individual zone approaches equilibrium and produces stars at nearly the same metallicity over several Gyr. This property is evident in the nearly vertical evolutionary tracks in the lower left panel and the nearly horizontal  $[\text{O}/\text{H}]$ - $\log(\text{age})$  relations in the upper right panel. One can mitigate this effect by allowing  $\eta$  to slowly decrease in time, so that the equilibrium abundance itself grows steadily with time. We have experimented with this type of model, adapting the procedure described by equations 115 and 116 of WAF17 to construct analytic solutions in which  $(1 + \eta - r)$  decreases linearly in each annulus over  $t = 0 - 12$  Gyr. With continuously increasing  $[\text{O}/\text{H}]$  in individual zones we are able to get a slightly better match to the observed  $[\text{O}/\text{H}]$ - $\log(\text{age})$  distribution, but in our limited explorations we still have not found a model that produces a median age below 4 Gyr near solar metallicity. These models still have smooth star formation histories, and it could be that star formation bursts or the vertical selection effect mentioned above are crucial for reproducing these APOGEE results.

There are several directions for improving this kind of multi-zone modeling. One is to carry out more systematic sampling of the high-dimensional parameter space, e.g. via Markov Chain Monte Carlo, which requires first deciding on a figure of merit for evaluating agreement with observations. This approach might involve forward-modeling the impact of observational errors instead of Bayesian inference of age-distribution parameters as an intermediate step. A second direction is to use numerical simulation predictions as a source of informed priors for radial migration prescriptions and parameter ranges. A third direction, probably essential for breaking parameter degeneracies, is to expand the set of observational constraints, including MDFs and  $[\alpha/\text{Fe}]$ - $[\text{Fe}/\text{H}]$  tracks as a function of Galactic position (Hayden et al. 2015), present-day ISM abundance gradients, and age-abundance distributions over a wider range of the disc. Robust inferences must account for uncertainties in IMF-

averaged yields and SNIa DTDs, and improving external constraints on these quantities would mitigate degeneracies with chemical evolution parameters that describe outflows, star formation efficiency, and star formation histories. We anticipate progress along all of these directions in future work. The difficulty of finding a fully successful fit to the data even with the many adjustable parameters of our mixture model implies that any *ab initio* model that reproduces the measured age-abundance distributions with few or no adjustments has scored a significant success.

## 4.2 Chempy model

*Chempy* (Rybizki, Just & Rix 2017, hereafter R17) is a flexible, open-source code developed for modeling Galactic chemical evolution. It incorporates detailed predictions for the yields of many chemical elements based on the prescriptions of Karakas (2010), Nomoto, Kobayashi & Tominaga (2013), and Seitzzahl et al. (2013) for asymptotic giant branch (AGB), core-collapse supernovae, and Type Ia supernovae feedback respectively (the “default” yield set). An “alternative” yield set instead uses the prescriptions of Ventura et al. (2013), Chieffi & Limongi (2004), and Thielemann et al. (2003) for these three enrichment processes. The code functions in a Bayesian framework to constrain physical parameters that describe the star formation efficiency, the star formation history, the outflow efficiency, and the initial mass of the gaseous corona. It simultaneously constrains parameters that describe the stellar and supernova population, namely the high mass slope of the IMF, the minimum delay time for SNIa, and the normalisation of the SNIa DTD (assumed to have a  $t^{-1.1}$  form). R17 infer optimal parameter values by fitting the detailed chemical abundance pattern of the Sun, or Arcturus, or present-day B-stars, together with the observed CCSN/SNIa ratio from Mannucci et al. (2005) and the coronal metallicity measured by Fox et al. (2016). Here we compare to their “Sun+” model computed with both the default and alternative yield sets and their “Arcturus+” models computed with the default yield set (see Table 4 or R17 for parameter values). These are one-zone models; R17 also construct a multi-zone model in which the solar, Arcturus, and B-star abundances are fit simultaneously with the same stellar population parameters but with independent star formation and outflow parameters to represent different birth zones.

In the terminology of the previous section, the parameters of the Sun+ model correspond approximately to  $\tau_* = 2$  Gyr,  $\eta = 1$ , and a linear-exponential SFH with  $\tau_{\text{sfh}} = 3$  Gyr. However, while the WAF17 models assume primordial composition infall, the R17 models have metal exchange between the ISM and the corona. More importantly, the R17 models incorporate nucleosynthesis predictions for many elements, including metallicity dependent yields. Although R17 predict significant AGB contributions to C and N, we do not include those in our comparison here because the models do not incorporate internal mixing on the giant branch. The predicted AGB contributions to the other elements considered here are below 10 per cent, far below in most cases (see Fig. 13 of R17).

Fig. 18 shows the [M/H]-age relation from Fig. 3 with the R17 GCE model predictions overplotted as lines. The Sun+ model with the default yield set gives the best match

to the  $[\alpha/\text{M}]$ -age relation, and its evolutionary track in the  $[\alpha/\text{M}]$ -[M/H] plane is similar to the observed low- $[\alpha/\text{M}]$  sequence. The predicted drop in  $[\alpha/\text{M}]$  is faster at early times than the observations imply, which suggests that SNIa iron enrichment is becoming important too quickly. The Arcturus-normalised models predict only a small drop in  $[\alpha/\text{M}]$  with time, which is due to its lower fractional SNIa contribution to iron-peak elements. They yield a poor match to the observations, but qualitatively the behavior is similar to the one-zone WAF17 models. In particular, the Arcturus model is very similar to the inner-most WAF17 model. The predicted tracks of [M/H]-age and [O/H]-age resemble those of the one-zone models in Fig. 13, and like those models they do not reproduce the observed increase of mean age above solar metallicity. All three models approach solar [O/H] too quickly, and the Sun+ model also rises too quickly in [M/H].

Fig. 19 and 20 show the comparisons to the R17 GCE models for the individual elements. These figures are the same as Fig. 8 through 11, with the three *Chempy* models overplotted for both the age and [X/M] vs [M/H] distributions. Rather than discuss individual element comparisons, we make a few general observations, focusing on the Sun+ model. For the  $\alpha$  elements, the predicted [X/M]-age tracks differ in the normalisation at early times, which reflects the CCSN yield ratios relative to solar values, and in the drop between this initial ratio and the late-time ratio, which mainly reflects the relative contribution of SNIa to this element. In particular, the predicted SNIa contribution is negligible for O and Mg but significant for Si, S, Ca, and Ti (see Fig. 13 of R17), so these elements show a smaller predicted drop. However, the element-by-element variations predicted by *Chempy* do not produce good agreement with the APOGEE data. The observed [X/M]-age relations for the  $\alpha$  elements are fairly similar for the most part, and to the extent that they differ it is not in the ways predicted by the models.

For light odd-Z elements, the R17 models predict a rapid rise in [X/M] at early times because of metallicity-dependent yields, followed by a plateau in [X/M] at late times. However, the models predict very few stars at the immediate start of star formation, therefore the sharp rise and peak would not be observable in the stellar population. The R17 models are not consistent with the [X/M]-[M/H] distributions of the data. The observed age trends for Al and K qualitatively resemble the observed (and predicted) trends for  $\alpha$  elements rather than the flat predictions for odd-Z elements. This disagreement suggests that the yield models predict overly strong metallicity dependence, and that CCSN or some other nucleosynthetic source produce light odd-Z elements even when the metallicity of the stellar population is low.

For Mn and Ni the model predictions again rise at early times because of metallicity-dependent yields. The predicted [Mn/M]-age and [Mn/M]-[M/H] trends are in strikingly good agreement with the data, the best match found in these figures. As mentioned in Section 3.5, NLTE corrections could be important for [Mn/M], in which case this good agreement would be a coincidence. As mentioned in §3.5, the theoretical Ni trend does not agree with the observed trend. The models predict a shallow trend of [Ni/M] with age that is opposite in direction to the observed shallow trend. This discrepancy could reflect incorrect metallicity-dependence of

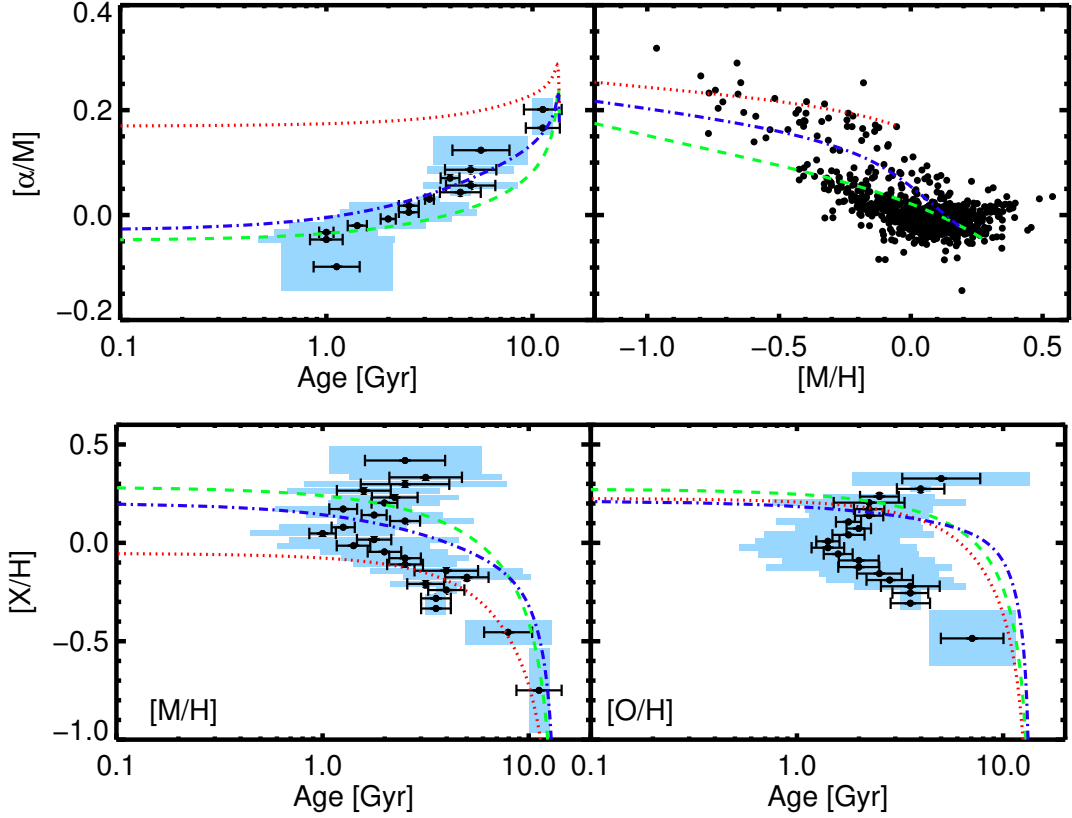


**Figure 18.** The upper left panel and both bottom panels are the same as Fig. 2 and 3, but showing the observed age-abundance relation for  $[\alpha/M]$ ,  $[M/H]$ , and  $[O/H]$ , as well as  $[\alpha/M]$  vs  $[M/H]$  with the R17 GCE models shown. The lines are the results of the R17 GCE model using the default yields fit to the Sun (dashed green) and Arcturus (dotted red), and the alternative yield set fit to the Sun (dash-dotted blue).

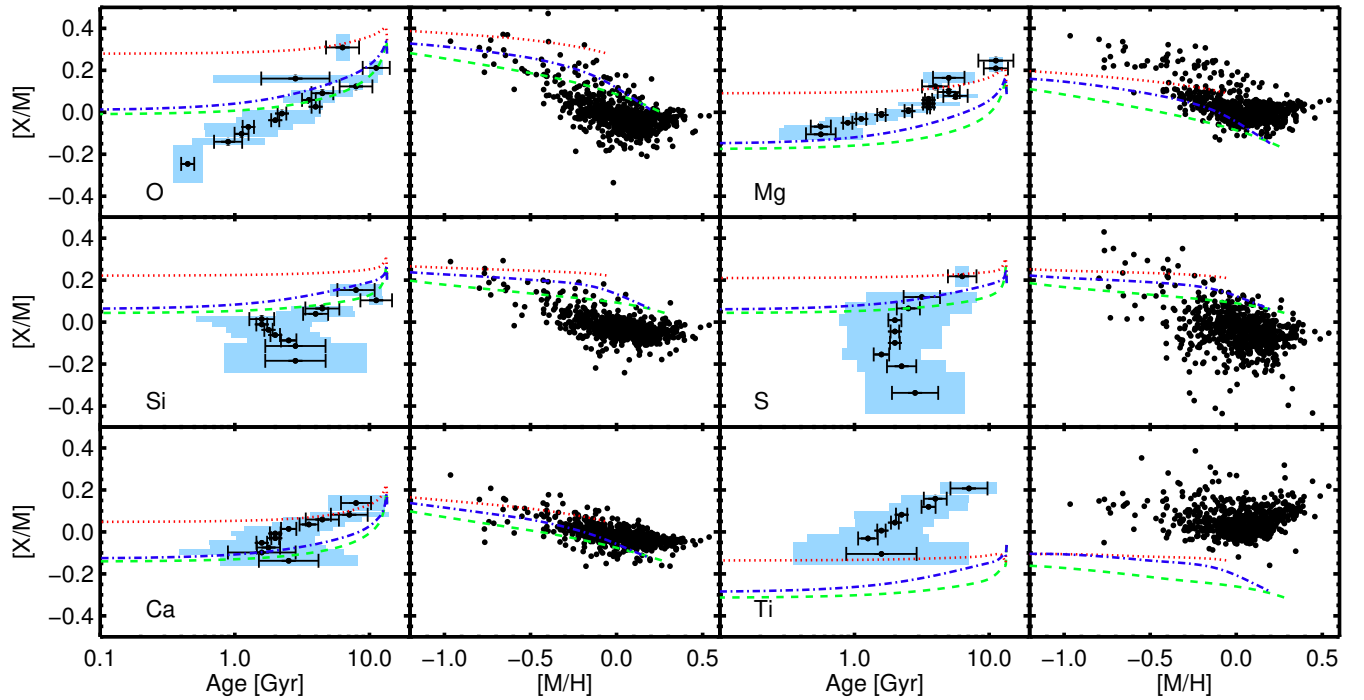


**Figure 19.** Same as Fig. 8 for all  $\alpha$ -elements comparing to GCE models. The lines are the results of the R17 GCE model using the default yields fit to the Sun (dashed green) and Arcturus (dotted red), and the alternative yield set fit to the Sun (dash-dotted blue).

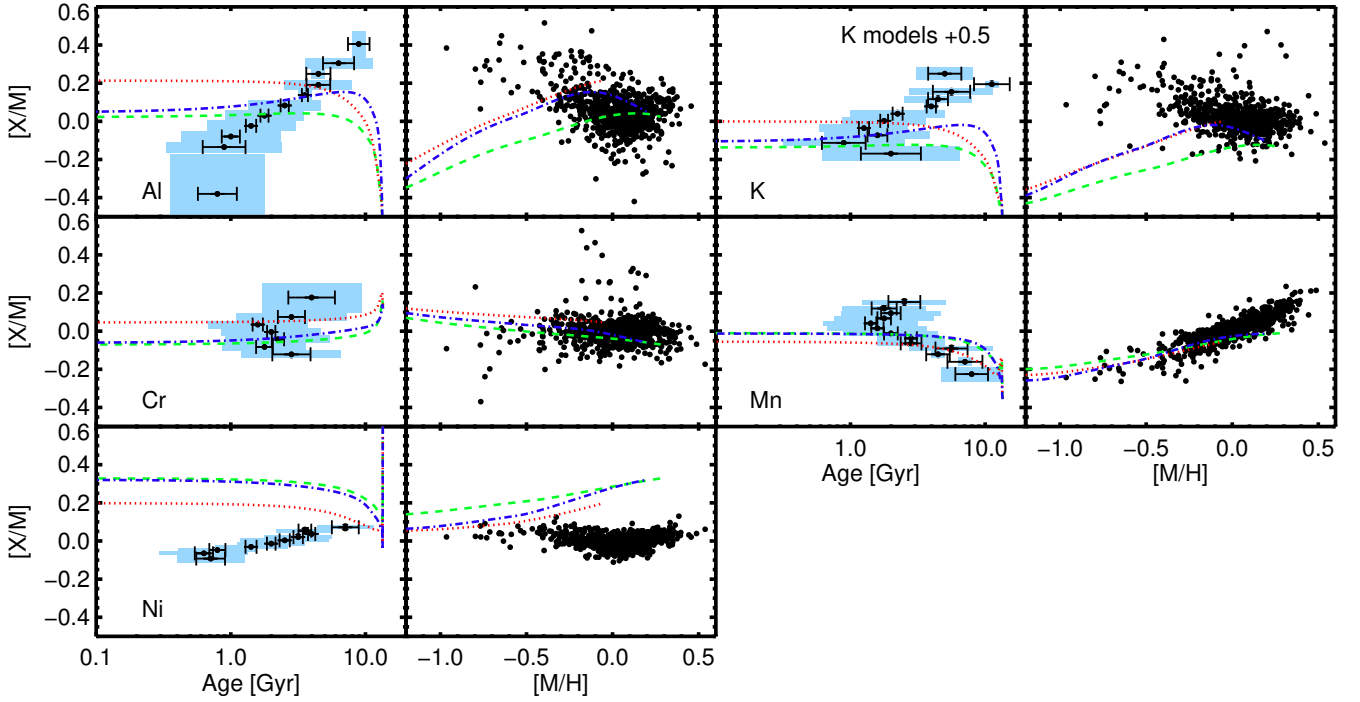


**Figure 20.** Same as Fig. 8 for the light odd-Z and Fe-peak elements comparing to GCE models. The lines are the results of the R17 GCE model using the default yields fit to the Sun (dashed green) and Arcturus (dotted red), and the alternative yield set fit to the Sun (dash-dotted blue).

Ni yields in the models, or a CCSN contribution to Ni that is too small, or both.

R17 find that the observed solar abundance pattern, CCSN/SNIa ratio, and corona metallicity are sufficient to provide interestingly tight constraints on the seven parameters of their one-zone chemical evolution model. The poor agreement with the observed abundance-age relations found here indicates that these models are still missing one or more physical ingredients that have a major impact on these relations. The analysis of §4.1 suggests that radial mixing of stellar populations is at least one of those ingredients. However, the relative behaviour of different elements depends largely on yields, and the disagreements in Fig. 19-?? probably indicate that even the most sophisticated current nucleosynthesis calculations still have substantial errors for some elements.

## 5 CONCLUSIONS

As described in F16, ages of red giant stars can be determined through Bayesian isochrone matching with 0.16 dex uncertainty if the distances are known precisely. However, these age uncertainties, as well as those possible for CN ages ( $\sim 0.20$  dex), are still high for examining detailed age trends across the Galactic disc using individual stars. In this work, we use the hierarchical modelling technique described in F16 to model the SFH of our sample of local red giants as a function of individual elemental abundances and present age-abundance trends for the solar neighbourhood. Using APOGEE DR14 parameters, we confirm the steeply increasing  $[\alpha/M]$ -age trend found in F16, and also present

age trends for the overall metallicity and 17 individual elements. We do note that our analysis does not account for any possible systematic uncertainties due to the spectroscopic methods or the stellar models.

Using both  $[M/H]$  and  $[O/H]$ , we find that the most metal-rich stars in our sample are older than the solar metallicity stars. This behavior is consistent with the  $[\alpha/M]$ -age relation and the  $[\alpha/M]$  vs  $[M/H]$  distribution of the sample. The solar metallicity bins contain stars with a large range of  $[\alpha/M]$  abundances, including the lowest, sub-solar  $[\alpha/M]$  stars, while the highest metallicity bins have a smaller range in  $[\alpha/M]$  abundances centred around solar. Through modeling the SFH of stars binned in both  $[M/H]$  and  $[\alpha/M]$  we find that the metal-rich stars have a gradient in age with  $[\alpha/M]$  at each  $[M/H]$ . At any given  $[M/H]$  the high- $[\alpha/M]$  stars are older than the low- $[\alpha/M]$  stars. However, the youngest stars are still those with solar metallicity and sub-solar  $[\alpha/M]$ . As these are the youngest stars, they are the most likely to have formed at the solar radius. Because the metal-rich, solar  $[\alpha/M]$  stars are older, they probably did not form in the solar neighbourhood. They could have radially migrated from elsewhere, perhaps the inner disc, where star formation occurred more rapidly and perhaps started earlier, resulting in high metal content of the ISM at earlier times.

We confirm the strong age-abundance trends of C and N in giant stars due to internal mixing discussed in work by Masseron & Gilmore (2015) and Martig et al. (2016). Our  $[C/N]$ -age relation using ages derived independently of the C and N abundance suggests the minimum uncertainty in the age derived using the CN abundance technique is approximately 0.2 dex in  $\log(\text{age})$ . The age trends of the individual  $\alpha$ -elements are consistent with the overall  $[\alpha/M]$

trend, and are especially tight and steep in O and Mg. Si and Ca deviate from the  $[\alpha/M]$  trend in the lowest abundance ratio bins, and S has a very broad distribution with only a weak age trend in the highest and lowest abundance ratio bins. Al and K have  $\alpha$ -like age trends, while the Na and P trends are consistent with flat or weakly decreasing in age with abundance ratio. V, Cr, and Co also have flat age-abundance ratio trends. Mn has an age trend that is very similar to  $[M/H]$  and Ni has a very tight,  $\alpha$ -like behavior.

These observations are crucial for providing strong constraints on the parameters of GCE models. As we show with the comparisons to WAF17 analytic GCE models and the flexible ‘leaky box’ GCE model *Chempy* from R17, single zone models cannot reproduce the full age-abundance sequences. Using the WAF17 models, a mixture model of five single zones can reproduce the continuous age- $[\alpha/M]$  trend but not large age dispersion in the high  $[\alpha/M]$  stars. The mixture model is able to produce super-solar metallicity stars with older ages than the mean age of the solar metallicity stars. However, the mean age of the solar metallicity stars is not as young as the observations and the mean age does not increase smoothly with increasing metallicity. The Sun+ model of R17 is consistent with the shape of most of the  $\alpha$ -elements for the higher abundances, but flattens out at younger ages. The observations, for most elements, maintain a constant slope or turn over and increase in age at lower abundance ratios. This is particularly striking in the case of  $[M/H]$  and  $[Mn/M]$  for which the *Chempy* models are consistent with the lower abundance bins, but flatten while the observations turn over and increase with age at higher abundances. These comparisons add evidence in support of the picture that individual abundances of stars currently in the solar neighbourhood cannot be modelled as a single evolutionary zone, but actually some of these stars were born in different environments and over time migrated to the solar neighbourhood. In this sense the multi-zone analytic models are a bit more instructive in constraining the parameters of chemical evolution elsewhere in the disc. These comparisons also highlight the potential of using variations in the abundance-age trends of different elements, even among the same element-groups, to help disentangle the effects of Galactic evolution.

Although observations of the solar neighbourhood are continuing to find an interesting and diverse population of local stars, such detailed observations are needed in farther regions of the Galactic disc to form a more complete picture of the evolutionary history of the Milky Way. Giant stars are excellent tracers of the disc populations and can be observed to farther distances than many other stellar types. Using statistical methods such as those presented in F16, age trends are now possible for large samples of giant stars with precise atmospheric parameters and distances. Such observations will be available for a large sample of the Milky Way disc from APOGEE and Gaia data.

## ACKNOWLEDGEMENTS

We thank the anonymous referee for their helpful comments and suggestions. D.K.F. acknowledges funds from the Alexander von Humboldt Foundation in the framework of the Sofja Kovalevskaja Award endowed by the Federal

Ministry of Education and Research. J.B. acknowledges the support of the Natural Sciences and Engineering Research Council of Canada (NSERC), funding reference number RGPIN-2015-05235, and from an Alfred P. Sloan Fellowship. DAGH and OZ acknowledge support provided by the Spanish Ministry of Economy and Competitiveness (MINECO) under grant AYA-2014-58082-P.

Funding for the Sloan Digital Sky Survey IV has been provided by the Alfred P. Sloan Foundation, the U.S. Department of Energy Office of Science, and the Participating Institutions. SDSS-IV acknowledges support and resources from the Center for High-Performance Computing at the University of Utah. The SDSS web site is [www.sdss.org](http://www.sdss.org).

SDSS-IV is managed by the Astrophysical Research Consortium for the Participating Institutions of the SDSS Collaboration including the Brazilian Participation Group, the Carnegie Institution for Science, Carnegie Mellon University, the Chilean Participation Group, the French Participation Group, Harvard-Smithsonian Center for Astrophysics, Instituto de Astrofísica de Canarias, The Johns Hopkins University, Kavli Institute for the Physics and Mathematics of the Universe (IPMU) / University of Tokyo, Lawrence Berkeley National Laboratory, Leibniz Institut für Astrophysik Potsdam (AIP), Max-Planck-Institut für Astronomie (MPIA Heidelberg), Max-Planck-Institut für Astrophysik (MPA Garching), Max-Planck-Institut für Extraterrestrische Physik (MPE), National Astronomical Observatories of China, New Mexico State University, New York University, University of Notre Dame, Observatório Nacional / MCTI, The Ohio State University, Pennsylvania State University, Shanghai Astronomical Observatory, United Kingdom Participation Group, Universidad Nacional Autónoma de México, University of Arizona, University of Colorado Boulder, University of Oxford, University of Portsmouth, University of Utah, University of Virginia, University of Washington, University of Wisconsin, Vanderbilt University, and Yale University. Collaboration Overview Start Guide Affiliate Institutions Key People in SDSS Collaboration Council Committee on Inclusiveness Architects Survey Science Teams and Working Groups Publication Policy How to Cite SDSS External Collaborator Policy

## REFERENCES

- Abolfathi B., et al., 2017, preprint, ([arXiv:1707.09322](https://arxiv.org/abs/1707.09322))  
 Adibekyan V., et al., 2016, *Astronomy & Astrophysics*, 592, A87  
 Allende Prieto C., Beers T. C., Wilhelm R., Newberg H. J., Rockosi C. M., Yanny B., Lee Y. S., 2006, *The Astrophysical Journal*, 636, 804  
 Anders F., et al., 2017, *Astronomy & Astrophysics*, 597, A30  
 Anderson E., Francis C., Street I., Road E., 2012, *Astronomy Letters*, 2, 1  
 Andrews B. H., Weinberg D. H., Schönrich R., Johnson J. A., 2017, *The Astrophysical Journal*, 835, 224  
 Battistini C., Bensby T., 2015, *Astronomy & Astrophysics*, 577, A9  
 Bedell M., et al., 2018, preprint, ([arXiv:1802.02576](https://arxiv.org/abs/1802.02576))  
 Bensby T., Feltzing S., Oey M. S., 2014, *Astronomy & Astrophysics*, 562, A71  
 Bergemann M., et al., 2014, *Astronomy & Astrophysics*, 565, A89  
 Bird J. C., Kazantzidis S., Weinberg D. H., 2012, *Monthly Notices of the Royal Astronomical Society*, 420, 913  
 Bird J. C., Kazantzidis S., Weinberg D. H., Guedes J., Callegari



- S., Mayer L., Madau P., 2013, *The Astrophysical Journal*, 773, 43
- Blanton M. R., et al., 2017, *The Astronomical Journal*, 154, 28
- Bovy J., Rix H.-w., Liu C., Hogg D. W., Beers T. C., Lee Y. S., 2012, *The Astrophysical Journal*, 753, 148
- Bovy J., Rix H.-w., Schlafly E. F., Nidever D. L., Holtzman J. A., Shetrone M., Beers T. C., 2016, *The Astrophysical Journal*, 823, 30
- Brown A. G. A., 2017, preprint, ([arXiv:1709.01216](https://arxiv.org/abs/1709.01216))
- Casagrande L., Schönrich R., Asplund M., Cassisi S., Ramírez I., Meléndez J., Bensby T., Feltzing S., 2011, *Astronomy & Astrophysics*, 530, A138
- Chabrier G., 2001, *The Astrophysical Journal*, 554, 1274
- Chaplin W. J., et al., 2011, *Science*, 332, 213
- Chiappini C., Matteucci F., Gratton R., 1997, *The Astrophysical Journal*, 477, 765
- Chiappini C., et al., 2015, *Astronomy & Astrophysics*, 576, L12
- Chieffi A., Limongi M., 2004, *The Astrophysical Journal*, 608, 405
- Dalcanton J. J., 2007, *The Astrophysical Journal*, 658, 941
- De Silva G. M., et al., 2015, *Monthly Notices of the Royal Astronomical Society*, 449, 2604
- Dziembowski W. A., Fiorentini G., Ricci B., Sienkiewicz R., 1999, *Astronomy & Astrophysics*, 343, 990
- Edvardsson B., Andersen J., Gustafsson B., Lambert D. L., Nissen P. E., Tomkin J., 1993, *Astronomy and Astrophysics Supplement Series*, 102
- Feltzing S., Howes L. M., McMillan P. J., Stokute E., 2017, *Monthly Notices of the Royal Astronomical Society: Letters*, 465, L109
- Feillet D. K., Bovy J., Holtzman J., Girardi L., MacDonald N., Majewski S. R., Nidever D. L., 2016, *The Astrophysical Journal*, 817, 40
- Finlator K., Davé R., 2008, *Monthly Notices of the Royal Astronomical Society*, 385, 2181
- Fox A. J., et al., 2016, *The Astrophysical Journal Letters*, 816, L11
- Freeman K., et al., 2012, *Monthly Notices of the Royal Astronomical Society*, 428, 3660
- Gaia Collaboration et al., 2016, *Astronomy & Astrophysics*, 595, A1
- García Pérez A. E., et al., 2016, *The Astronomical Journal*, 151, 144
- Gilmore G., et al., 2012, *The Messenger*, 147, 25
- Gunn J. E., et al., 2006, *The Astronomical Journal*, 131, 2332
- Hawkins K., Masseron T., Jofré P., Gilmore G., Elsworth Y., Hekker S., 2016, *Astronomy & Astrophysics*, 594, A43
- Hayden M. R., et al., 2015, *The Astrophysical Journal*, 808, 132
- Hayden M. R., Recio-Blanco A., de Laverny P., Mikolaitis S., Worley C. C., 2017, *Astronomy & Astrophysics*, 608, L1
- Haywood M., Di Matteo P., Lehnert M. D., Katz D., Gómez A., 2013, *Astronomy & Astrophysics*, 560, A109
- Ho A. Y. Q., Rix H.-W., Ness M. K., Hogg D. W., Liu C., Ting Y.-S., 2017, *The Astrophysical Journal*, 841, 40
- Holtzman J. A., et al., 2015, *The Astronomical Journal*, 150, 148
- Iben Jr. I., 1965, *The Astrophysical Journal*, 142, 1447
- Jia Y. P., Chen Y. Q., Zhao G., Bari M. A., Zhao J. K., Tan K. F., 2018, *Monthly Notices of the Royal Astronomical Society*, 473, 2622
- Jofré P., et al., 2016, *Astronomy & Astrophysics*, 595, A60
- Karakas A. I., 2010, *MNRAS*, 403, 1413
- Kobayashi C., Umeda H., Nomoto K., Tominaga N., Ohkubo T., 2006, *The Astrophysical Journal*, 653, 1145
- Kroupa P., 2001, *Monthly Notices of the Royal Astronomical Society*, 322, 231
- Lagarde N., Decressin T., Charbonnel C., Eggenberger P., Ekström S., Palacios A., 2012, *Astronomy & Astrophysics*, 543, A108
- Lagarde N., Robin A. C., Reylé C., Nasello G., 2017, *Astronomy & Astrophysics*, 601, A27
- Lindegren L., et al., 2016, *Astronomy & Astrophysics*, 595, A4
- Loebman S. R., Roškar R., Debattista V. P., Ivezić Ž., Quinn T. R., Wadsley J., 2011, *The Astrophysical Journal*, 737, 8
- Loebman S. R., Debattista V. P., Nidever D. L., Hayden M. R., Holtzman J. A., Clarke A. J., Roškar R., Valluri M., 2016, *The Astrophysical Journal*, 818, L6
- Mackereth J. T., et al., 2017, *Monthly Notices of the Royal Astronomical Society*, 471, 3057
- Majewski S. R., et al., 2017, *The Astronomical Journal*, 154, 94
- Mannucci F., Della Valle M., Panagia N., Cappellaro E., Cresci G., Maiolino R., Petrosian A., Turatto M., 2005, *A&A*, 433, 807
- Maoz D., Mannucci F., Brandt T. D., 2012, *Monthly Notices of the Royal Astronomical Society*, 426, 3282
- Martell S. L., et al., 2017, *Monthly Notices of the Royal Astronomical Society*, 465, 3203
- Martig M., et al., 2015, *Monthly Notices of the Royal Astronomical Society*, 451, 2230
- Martig M., et al., 2016, *Monthly Notices of the Royal Astronomical Society*, 456, 3655
- Masseron T., Gilmore G., 2015, *Monthly Notices of the Royal Astronomical Society*, 453, 1855
- Masseron T., Lagarde N., Miglio A., Elsworth Y., Gilmore G., 2017, *Monthly Notices of the Royal Astronomical Society*, 464, 3021
- Minchev I., Chiappini C., Martig M., 2013, *Astronomy & Astrophysics*, 558, A9
- Ness M., Hogg D. W., Rix H.-W., Martig M., Pinsonneault M. H., Ho A. Y. Q., 2016, *The Astrophysical Journal*, 823, 114
- Nidever D. L., et al., 2015, *The Astronomical Journal*, 150, 173
- Nieva M.-F., Przybilla N., 2012, *Astronomy & Astrophysics*, 539, A143
- Nissen P. E., 2015, *Astronomy & Astrophysics*, 579, A52
- Nissen P. E., Silva Aguirre V., Christensen-Dalsgaard J., Collet R., Grundahl F., Slumstrup D., 2017, *Astronomy & Astrophysics*, 608, A112
- Nomoto K., Kobayashi C., Tominaga N., 2013, *ARA&A*, 51, 457
- Nordlander T., Lind K., 2017, *Astronomy & Astrophysics*, 607, A75
- Nordström B., et al., 2004, *Astronomy & Astrophysics*, 1019, 989
- Ramírez I., Allende Prieto C., Lambert D. L., 2013, *The Astrophysical Journal*, 764, 78
- Randich S., Gilmore G., Consortium G.-E., 2013, *The Messenger*, 154, 47
- Roškar R., Debattista V. P., Quinn T. R., Stinson G. S., Wadsley J., 2008, *The Astrophysical Journal*, 684, L79
- Rybicki J., Just A., Rix H.-W., 2017, *Astronomy & Astrophysics*, 605, A59
- Salaris M., Pietrinferni A., Piersimoni A. M., Cassisi S., 2015, *Astronomy & Astrophysics*, 583, A87
- Schönrich R., Binney J., 2009, *Monthly Notices of the Royal Astronomical Society*, 396, 203
- Seitzzahl I. R., et al., 2013, *MNRAS*, 429, 1156
- Sellwood J. A., Binney J. J., 2002, *MNRAS*, 336, 785
- Shetrone M., et al., 2015, *The Astrophysical Journal Supplement Series*, 221, 24
- Slumstrup D., Grundahl F., Brogaard K., Thygesen A. O., Nissen P. E., Jessen-Hansen J., Van Eylen V., Pedersen M. G., 2017, *Astronomy & Astrophysics*, 604, L8
- Smiljanic R., et al., 2016, *Astronomy & Astrophysics*, 589, A115
- Snaith O. N., Haywood M., Di Matteo P., Lehnert M. D., Combes F., Katz D., Gómez A., 2014, *The Astrophysical Journal*, 781, L31
- Spina L., Meléndez J., Karakas A. I., Ramírez I., Monroe T. R., Asplund M., Yong D., 2016, *Astronomy & Astrophysics*, 593, A125
- Tayar J., et al., 2015, *Astrophysical Journal*, 807, 82

- Thielemann F.-K., et al., 2003, *Nuclear Physics A*, 718, 139
- Van Eck S., Neyskens P., Jorissen A., Goriely S., Siess L., Plez B., 2015, in *EAS Publications Series*. pp 339–342, doi:10.1051/eas/1571080
- Ventura P., Di Criscienzo M., Carini R., D’Antona F., 2013, *MNRAS*, 431, 3642
- Weinberg D. H., Andrews B. H., Freudenburg J., 2017, *The Astrophysical Journal*, 837, 183
- Wielen R., Fuchs B., Dettbarn C., 1996, *Astronomy & Astrophysics*, 314, 438
- Wu Y., et al., 2017, preprint, ([arXiv:1712.09779](https://arxiv.org/abs/1712.09779))
- Zamora O., et al., 2015, *The Astronomical Journal*, 149, 181
- Zasowski G., et al., 2013, *The Astronomical Journal*, 146, 81
- da Silva R., Porto de Mello G. F., Milone A. C., da Silva L., Ribeiro L. S., Rocha-Pinto H. J., 2012, *Astronomy & Astrophysics*, 542, A84
- van Leeuwen F., 2007, *Astronomy and Astrophysics*, 474, 653

This paper has been typeset from a  $\text{\TeX}/\text{\LaTeX}$  file prepared by the author.